

1 Modeling the magnetospheric X-ray emission from
2 solar wind charge exchange with verification from
3 XMM-Newton observations

Ian C. Whittaker,¹ Steve Sembay,¹ Jennifer A. Carter,¹ Andrew M. Read,¹

Steve E. Milan,¹ Minna Palmroth,²

Corresponding author: I. Whittaker, Department of Physics and Astronomy, University of
Leicester, University Road, Leicester LE1 7RH, UK. (iw47@le.ac.uk)

¹Department of Physics and Astronomy,
University of Leicester, Leicester, United
Kingdom.

²Finnish Meteorological Institute, Helsinki,
Finland.

Key Points.

- MHD based simulations provide a viable alternative to empirical modeling of X-ray emissivity.
- SWCX enhancement variance strongly depends on the accuracy of the heavy ion abundance.
- Modeled X-ray emissivity provides global imaging of the magnetosheath.

4 **Abstract.** An MHD based model of terrestrial solar wind charge exchange
5 (SWCX) is created and compared to 19 case study observations in the 0.5-
6 0.7 keV emission band taken from the EPIC cameras onboard XMM-Newton.
7 This model incorporates the GUMICS-4 MHD code and produces an X-ray
8 emission datacube from O^{7+} and O^{8+} emission lines around the Earth using
9 in-situ solar wind parameters as the model input. This study details the modeling
10 process and shows that fixing the oxygen abundances to a constant value reduces
11 the variance when comparing to the observations, at the cost of a small accuracy
12 decrease in some cases. Using the ACE oxygen data returns a wide ranging
13 accuracy, providing excellent correlation in a few cases and poor/anti correlation
14 in others. The sources of error for any user wishing to simulate terrestrial
15 SWCX using an MHD model are described here and include mask position,
16 hydrogen to oxygen ratio in the solar wind and charge state abundances. A
17 dawn-dusk asymmetry is also found, similar to the results of empirical modeling.
18 Using constant oxygen parameters, magnitudes approximately double that
19 of the observed count rates are returned. A high accuracy is determined between
20 the model and observations when comparing the count rate difference between
21 enhanced SWCX and quiescent periods.

1. Introduction

22 The terrestrial solar wind charge exchange process involves the liberation and capture
23 of an electron from a neutral species at the Earth (i.e., hydrogen) to a heavy, high
24 charge state, ion in the solar wind. The electron can be captured in an excited state and
25 transition to lower energy states via photon emission; which in the cases of X-ray photons,
26 is detectable by X-ray telescopes [e.g. *Cravens et al.*, 2001; *Henley and Shelton*, 2008].
27 X-ray charge exchange is a non-thermal emission, which was first detected in Röntgen-
28 Satellit (ROSAT) observations of comets, when the solar wind interacted with the neutral
29 gas outflow [*Lisse et al.*, 1996; *Cravens*, 1997]. Quantification of the X-ray emission has
30 focussed on highly ionised oxygen [e.g. *Koutroumpa*, 2012] as most space based X-ray
31 observatories investigate photon energies around $\frac{3}{4}$ keV and have observed SWCX in this
32 energy range, including XMM-Newton [e.g. *Snowden et al.*, 2004], Suzaku [*Ishikawa et al.*,
33 2013] and Chandra [*Slavin et al.*, 2013]. More recent attempts at quantifying charge
34 exchange from other ions with emission lines around the $\frac{1}{4}$ keV band have also been
35 performed, though the lack of cross sectional information for a number of faint transition
36 lines causes a high uncertainty in the results [*Kuntz et al.*, 2015]. This previous research
37 also showed a stronger correlation of the $\frac{1}{4}$ keV band ROSAT fluxes with solar wind flux
38 than the $\frac{3}{4}$ keV band.

39
40 Charge exchange emission has the possibility of being used as a powerful global imaging
41 tool [*Collier et al.*, 2012]. The peak charge exchange emission is expected to occur around
42 the subsolar magnetopause boundary where the pressure balance between the solar wind

43 and terrestrial atmosphere sits, thus allowing magnetopause, neutral hydrogen and plasma
44 dynamics models to be tested using a global view rather than via traditional in-situ
45 measurements [*Robertson et al.*, 2006; *Collier et al.*, 2010]. An example of the clear
46 boundary definition can be seen in panel e) of Figure 1. The magnetopause can be seen at
47 a subsolar distance of $9R_E$, while the bow shock sits at around $11R_E$. The charge exchange
48 process has previously been used for magnetopause modeling, using the resultant energetic
49 neutral atom emission from low charge state ions [e.g., *Collier et al.*, 2005; *Hosokawa et al.*,
50 2008; *Ogasawara et al.*, 2013]. Charge exchange X-ray emission has also been observed
51 at Venus [*Dennerl*, 2008], Mars [*Holmström et al.*, 2001] and the Moon [*Collier et al.*,
52 2014]. This indicates that for comparisons between the induced magnetospheres of the
53 unmagnetised planets and the Earth’s magnetosheath, X-ray charge exchange emission
54 could be a valuable tool. This is especially true with magnetopause modeling as the
55 movement of the boundary layer provides a proxy for monitoring the transfer of solar
56 wind energy into the magnetosphere [*Milan et al.*, 2004]. Hence, modeling and testing
57 of the terrestrial charge exchange process is necessary for understanding future imaging
58 studies.

59
60 The XMM-Newton observatory [*Jansen et al.*, 2001] was launched in 1999 and currently
61 moves in a highly elliptical orbit with a perigee altitude of ~ 7000 km and an apogee of
62 $\sim 114,000$ km, allowing long observation periods (~ 48 hour orbital period with 42 hours of
63 observations per orbit). The European Photon Imaging Camera (EPIC) onboard XMM-
64 Newton, contains two MOS CCD cameras [*Turner et al.*, 2001] and a single pn CCD
65 camera [*Strüder et al.*, 2001], which provides a spectral resolution of $\frac{\Delta E}{E} \sim 17$. We use

66 observations from the EPIC-MOS cameras in this study and all mention of EPIC data
67 refers to the MOS instruments. The EPIC-MOS cameras have a circular field of view
68 with a 30 arcminute (0.5°) diameter. While this field of view provides a high spatial
69 resolution at galactic distances, near the Earth this corresponds to ~ 60 km across the
70 camera. When we refer to SWCX we specifically mean the terrestrial emission. Our
71 main aim is to determine the efficacy of using a magnetohydrodynamic simulation, in
72 comparison to empirical models which have previously been used, to compare to observed
73 SWCX X-ray emission. *Kuntz et al.* [2015] showed that the Spreiter magnetopause model
74 [*Spreiter et al.*, 1966], typically used in empirical modeling of SWCX, underestimates
75 the magnetopause position. We use an MHD model for this comparative study and a
76 more recent magnetopause model. To determine the properties of the solar wind plasma
77 throughout the magnetosheath we use the GUMICS-4 (Global Unified Magnetosphere-
78 Ionosphere Coupling Simulation) MHD code [*Janhunen et al.*, 2012]. The process to
79 acquire and convert the MHD grid into an X-ray emissivity datacube is described in
80 Section 2. We then compare a line-of-sight integral through the datacube with the
81 observations made by the EPIC-MOS cameras in Section 3. Section 4 looks at improving
82 the correlation between observations and modeling, while Section 5 investigates the
83 influence of the oxygen related variables. We then provide our conclusions in Section 6.

2. Method

2.1. XMM-Newton EPIC observation cases

84 A systematic identification of observations affected by SWCX has been previously
85 determined for XMM-Newton up to revolution 1773 in August 2009 [*Carter et al.*, 2011].
86 These cases were found by searching for variability in the 0.5 to 0.7 keV band which

is primarily made up of O⁷⁺ and O⁸⁺ emission lines. Comparison of this variability in the oxygen $\frac{3}{4}$ keV band to the steady, source removed, continuum lightcurve of diffuse emission in the 2.5 to 5.0 keV band can indicate SWCX when the correlations between them are low [Carter and Sembay, 2008]. Table A.1 from Carter et al. [2011] lists 103 observations which are affected by SWCX in order of highest variability (χ_μ^2) between the steady continuum and oxygen band. We have chosen the top 30 observations (not including the comet cases), ranked by χ_μ^2 from 27.2 to 3.4 as the basis for this study. These cases are indicated as having the highest deviance between the X-ray background flux and oxygen emission. Table 1 gives the revolution number and observation identifiers for each of the selected cases, and we also include the date and the duration in hours.

2.2. Creating an X-ray emissivity cube

To create an X-ray emissivity grid for each timestep in the MHD model we use Equation (1) [Cravens, 2000]. This requires the combination of the GUMICS-4 MHD simulation output with both the neutral hydrogen number density and the alpha value (α), a scale factor containing the cross section of the charge exchange interaction.

$$P_X = \eta_H \eta_{SW} v_{av} \alpha \quad (1)$$

where:

P_X = emissivity (eV cm⁻³ s⁻¹)

η_{SW} = solar wind proton number density (cm⁻³)

η_H = neutral hydrogen number density (cm⁻³)

α = scale factor based on cross sectional data and oxygen abundance (eV cm²)

$$v_{av} = \sqrt{v_{sw}^2 + \frac{3k_B T}{m_p}} \quad (\text{cm s}^{-1})$$

2.2.1. The GUMICS-4 MHD model

As a first step to running the MHD model we require the upstream solar wind conditions as an input to the GUMICS-4 code. These solar wind parameters are downloaded from NASA's Space Physics Data Facility in the form of OMNI [King and Papitashvili, 2005] one minute resolution averages, a dataset taken from a combination of ACE, WIND and IMP 8 satellite data, and timeshifted to the bow-shock. The required input variables for GUMICS-4 are time (s), proton number density (m^{-3}), temperature ($^{\circ}\text{K}$), solar wind speed (v_x, v_y, v_z in m/s), and interplanetary magnetic field (B_x, B_y and B_z in T). In order to ensure a divergenceless solution, the IMF B_x component is kept constant. Missing data values in the OMNI data set have a linear interpolation applied to recover appropriate values for each timestep. We run the GUMICS-4 model using a four second timestep with a data output grid produced every five minutes (300s).

Once we have produced a set of MHD output datacubes for the duration of each XMM-Newton observation, we take a cuboid spatial subset covering the regions of interest (i.e., dayside magnetosheath). We define our irregular data grid with the highest spatial resolution closest to the planet, having limits of 0 to 15 R_E in GSE x and -18 to 18 R_E in GSE y and z in increasing intervals from 0.2 R_E up to 0.5 R_E . We use this grid in combination with the relevant GUMICS-4 output file to produce a datacube giving solar

128 wind proton number density, velocity and temperature for each GSE x , y and z grid value.

129

130 **2.2.2. The neutral hydrogen model**

131 We use the Hodges neutral hydrogen model [*Hodges, 1994*] to create a grid of neutrals
 132 in the same grid format as the GUMICS-4 data. The Hodges study used a Monte Carlo
 133 simulation process to model the hydrogen exosphere as a function of spherics. The values
 134 were given for four different solar radio flux values at 10.7 cm wavelength ($F_{10.7}$) at equinox
 135 and solstice, while also being dependent upon radial distance. During each case study we
 136 take the daily $F_{10.7}$ average and using the date of the observation, we interpolate between
 137 the four given $F_{10.7}$ values and the temporal distance from summer solstice using day-
 138 of-year number. This interpolation process produces a unique neutral hydrogen grid for
 139 each case study.

140

141 **2.2.3. Calculating α**

142 The alpha value is a proportional factor based on a combination of the relative
 143 abundances and the cross-section of each possible interaction between a solar wind ion
 144 and a neutral particle causing an emission line in the relevant energy range [*Cravens,*
 145 *2000*]. The general equation for the calculation of this value is shown in Equation (2),
 146 where X is the element required and q is the charge state.

$$147 \quad \alpha_{X^{q+}} = \sigma E \left[\frac{X^{q+}}{O} \right] \left[\frac{O}{H} \right] \quad (2)$$

148 In the case of calculating the oxygen emission lines we need to know the emission line
 149 energy, cross section of the interaction, abundance of the relevant charge state and the
 150 ratio of oxygen to hydrogen (O/H) in the solar wind. We use two hour time resolution,

151 O/H ratio and oxygen charge state abundance data from the ACE spacecraft, timeshifted
152 to the bow shock in the same way as the OMNI data. If no solar wind composition data
153 is available we use the values in *Schwadron and Cravens* [2000], which is discussed further
154 in Section 4.2.

155

156 The cross section value and energy for each transition of O^{7+} (seven transitions) and
157 O^{8+} (five transitions) with neutral hydrogen are based on experimental data taken from
158 *Bodewits* [2007]. The cross section value for each transition is interpolated based on the
159 input ion speed, from the five values given (200, 400, 600, 800, and 1000 kms^{-1}). The
160 individual alpha values for each transition are then summed to produce a combined alpha
161 value for all relevant oxygen transitions.

162

163 For comparison to empirical methods, the α value for the model timeframe shown in
164 Figure 1 is $7.6 \times 10^{-16} \text{ eV cm}^2$. This has been calculated based on the input solar wind
165 velocity of 438 km/s, an $\frac{O}{H}$ ratio of 1.1×10^{-3} , an O^{7+} abundance of 0.28, and an O^{8+}
166 abundance of 0.05. This value compares favourably with empirical α values of 6×10^{-16}
167 eV cm^2 [*Cravens et al.*, 2001; *Robertson and Cravens*, 2003].

168

169 **2.2.4. Combination of the data**

170 We now have all the requirements to produce an X-ray emissivity cube. The output of
171 the GUMICS-4 simulation is combined with both the neutral hydrogen number density
172 and the alpha value as shown in Equation 1. Example slices through the data grid for
173 each of the components which are combined to form the X-ray emissivity grid are given

174 in Figure 1. Each panel shows an example 2D slice through the 3D datacube in the
 175 ecliptic (x - y) plane at $z = 0$. Panels a) to c) of Figure 1 show GUMICS-4 data output
 176 of the solar wind proton number density, speed and temperature respectively. Panel d)
 177 shows a neutral hydrogen data slice from the Hodges model. Panel e) shows the result of
 178 combining the model output, neutral hydrogen data and cross section values together to
 179 create the model X-ray emissivity.

180

181 **2.2.5. Applying a mask**

182 As a one fluid simulation, the GUMICS-4 MHD code does not identify the difference
 183 between solar wind plasma and plasma of terrestrial origin. As a consequence we can
 184 observe high terrestrial plasma densities near the Earth which in turn produce unphysical
 185 X-ray emissivity. The terrestrial plasma does not contain the same ratio of highly ionized
 186 oxygen species and hence cannot produce the same level of charge exchange emission. We
 187 can clearly see this effect by comparing panels f) and g) of Figure 1 which are slices of panel
 188 e). In panel e) we present the x - y plane of X-ray emissivity which shows some emission
 189 enhancement very close to the Earth. When we examine the y - z plane with a cut taken
 190 at $x = 3.9 R_E$, in panel f), we see the extent of the terrestrial plasma. Panel g) shows a
 191 cut at $x = 9 R_E$ where the emission is not affected by the terrestrial plasma. The Earth
 192 size and position is also included in panels e), f) and g) for comparison. We assume the
 193 boundary between the terrestrial and solar wind plasmas is at the magnetopause [*Spreiter*
 194 *et al.*, 1966]. The magnetopause model given in *Shue et al.* [1998] defines this boundary,
 195 with all proton densities (panel a) within this region set to zero. The relative merits of
 196 the empirical and MHD based magnetopause are discussed in Section 4.1.

2.3. Calculating an estimated instrument view

197 We now have a three dimensional X-ray emissivity product in an irregular grid. To
198 simulate what XMM-Newton would see we integrate along the viewing path from the
199 satellite location. To determine the amount of X-ray emission directed along the line of
200 sight we integrate along the look vector, $\int P_X dS$, from Equation (1).

201

202 At every $0.5 R_E$ step distance through the data cube from the satellite location we take
203 an interpolated emissivity value. The nearest neighbor emissivity data points within a 0.5
204 R_E radial distance are taken and averaged, with each neighbor weighting dependent upon
205 the distance from the required point. This interpolated emissivity value is multiplied by
206 the step distance and totaled to create the integral column flux. While this integral energy
207 collection value can be used for comparison, as a final step we pass both the energy and
208 appropriate spectrum of the oxygen transitions through the EPIC instrument response
209 matrix to provide a counts per second (c/s) value in the 0.5 to 0.7 keV band. The start
210 and end times of each EPIC timestep (at 1000s resolution) can then be determined and
211 an appropriate average count rate for that specific time period returned. Shorter step
212 distances were also trialed, resulting in negligible flux differences due to the weighted
213 averaging method.

3. Results

214 An initial investigation of the 30 case studies showed that the EPIC camera suffered
215 from sparse data in six cases, which were removed from the study. Of the remaining 24
216 cases another five had XMM-Newton at a negative x value, i.e. antisunward, with an
217 instrument view direction that did not intersect our datacube and these cases were also

218 removed, leaving 19 case studies with data. Each case was assigned an identifying code,
219 comprising the year and number of the case within that year in date order (e.g. YY-C).
220 These identifiers have been included in Table 1.

3.1. Background removal

221 Processing of the raw EPIC data to produce the lightcurves used in this study is
222 described in detail in *Carter and Sembay* [2008]. This includes the methodology for
223 identifying and removing astrophysical point sources from the data and cleaning the data
224 of soft-proton flares which can produce a strongly variable diffuse background.

225
226 The residual diffuse signal is dominated by the variable foreground SWCX component
227 and background components which are non-variable on the timescale of individual
228 observations. This background is a combination of an X-ray component and the residual
229 particle background in the EPIC detectors. The background X-ray component is a
230 combination of the astrophysical X-ray background arising from emission from our Galaxy
231 and unresolved point sources (extragalactic active galactic nuclei), and from SWCX in
232 the wider heliosphere.

233
234 The particle background in each observation can be estimated by a well established
235 procedure [*Carter and Read*, 2007]. We have estimated the X-ray background from the
236 ROSAT all sky survey [*Voges et al.*, 1999]. For each look direction on the sky appropriate
237 to the EPIC data we have used existing procedures within NASA's HEASARC toolkit to
238 derive an estimated count rate in the EPIC instrument 0.5 to 0.7 keV energy band from
239 the observed count rate in the ROSAT R4 band, which has an energy range of between

240 0.44 and 1.01 keV. To make the conversion from one instrument to the other requires
241 the assumption of a spectral model. Formally the diffuse X-ray background spectrum is
242 well represented by a two-component thermal APEC model for the Galactic emission and
243 a power law for the unresolved power law [*Kuntz and Snowden, 2008*]. We have used
244 the spectral parameters from a deep analysis of case 01-3 previously studied by *Carter*
245 *et al.* [2010] modified by the appropriate absorption in the light-of-sight which is provided
246 by the HEASARC toolkit and derived from the Leiden/Argentine/Bohn (LAB) neutral
247 hydrogen survey [*Kalberla et al., 2005*]. Technically the spectral parameters will vary
248 according to sky position, however, the ROSAT to EPIC conversion in these bands is not
249 very sensitive to plausible variations in the parameters and the resultant uncertainty is
250 comparable to the uncertainty due to the inter-calibration between the instruments.

251

252 The total estimated background for each observation is listed in Table 1. In comparison
253 with the median observed count rate, also listed in Table 1, we can see that the background
254 (i.e. non local SWCX components) represents between $\sim 10\text{-}40\%$ of the observed 0.5 to
255 0.7 keV signal in these cases.

3.2. Observation to model comparison

256 For each case study we produce a full set of plots including the GUMICS-4 integral
257 energy and estimated count rate output, the solar wind conditions, the EPIC lightcurve,
258 and satellite positional information. These plots allow us to check for errors and notice
259 patterns in large count rate differences. An example of this type of plot is shown for
260 case 01-1 in Figure 2. The left hand panels show; the GUMICS-4 integral energy
261 output (a), the GUMICS-4 estimated count rate (b), the velocity and number density

262 of solar wind protons (c), B_z and dynamic pressure (d), the oxygen to hydrogen ratio
263 (e) and the oxygen state abundances (f). The right panels show; the observational
264 data (g), a comparison between GUMICS-4 and observations before background removal
265 (h), a comparison between GUMICS-4 and observations after background removal (i), a
266 normalized comparison (j), the radial distance of the satellite and magnetopause (k) and
267 the final smaller panels show the position, orbit path and look direction for the case.

268

269 The 01-1 case is of interest as it covers a long time period (26.5 hours), shows a wide
270 range of features, and was previously examined in detail by *Snowden et al.* [2004]. We see
271 good agreement between the background removed observations and the GUMICS-4 count
272 rates (panel i) from $\sim 15:00$ onwards, including a gradual decline in magnitude starting
273 around 22:00. The start of the case study suffers from an integral emissivity which is
274 several orders of magnitude in error (panel b). This is discussed further in Section 4.1
275 but results from the mask not accurately removing all the plasma of terrestrial origin.
276 Panel f) also shows a large variation of O^{7+} abundances, ranging from 10% to almost
277 50%, which is discussed in Section 4.2.

278

279 The GUMICS-4 count rate estimation comparison to the background reduced EPIC
280 observations, i.e. panel i), for all 19 cases are shown in Figures 3 and 4, with the respective
281 identification number from Table 1. To provide an initial comparison between the cases
282 we determine the median count rate of both the modeled and observed lightcurve and
283 take a ratio of the two. The magnitude ratios for each case varied between 0.11 and
284 20.9 with a median value of 1.65. This magnitude difference average is reasonable for

285 comparison although it is highly variable within cases, as observed in Figures 3 and 4.
286 The correlation between the two lightcurves was also calculated for each case, the average
287 for all cases was 0.07 with a standard deviation of 0.52. We discuss the importance and
288 large variance of these values in Section 4. The correlation, based on a zero time lag cross
289 correlation and normalized lightcurves, rather than covariance is used due to the large
290 magnitude differences indicated by the magnitude ratio limits.

4. Discussion

291 The average magnitude ratio between modeled and observed count rates of 1.65
292 indicates the model count rates are comparable to the observations although, as previously
293 mentioned, this comes with a large variability. We can compare this ratio to the empirical
294 study of *Carter et al.* [2011] who found less than a factor of ~ 2 in magnitude difference
295 for 50% of their cases. In our study we find only 6 of 19 cases (32%) within a factor of
296 two greater or smaller (i.e., a ratio between 0.5 and 2). This difference suggests that the
297 modeled process does a poorer job of magnitude modeling than the empirical study. The
298 correlation values are of concern with a mean value close to zero, due to 8 of the 19 cases
299 (42%) returning a negative correlation. These correlations can have high values and the
300 average absolute correlation value is returned as 0.44. In an attempt to determine why
301 the simulation of the X-ray emission is not reproducing the observations accurately we
302 investigate each of the model components, as set out in Section 2.2.

4.1. A re-examination of the method

303 From Equation (1), there are four important possible sources of error in our modeled
304 data; the MHD model, the neutral hydrogen model, the mask to remove the cold terrestrial

305 plasma, and the alpha value.

306
307 The GUMICS-4 model code has been verified in a one year study [*Gordeev et al.*, 2013]
308 and used in a range of other studies [e.g., *Hubert et al.*, 2006; *Palmroth et al.*, 2013]. The
309 requirements for the magnetospheric plasma simulation are well within the boundaries
310 set by GUMICS-4 of $\pm 64 R_E$ in y and z and up to $32 R_E$ in x . The main limitations
311 of the model, as described in *Janhunen et al.* [2012], are magnetotail reconnection and
312 near Earth plasma modeling ($< 3.7 R_E$). The first limitation is not relevant as we only
313 generate X-ray emission data at $x > 0$ and the second limitation is taken care of by use
314 of a magnetopause position mask. It is also important to note that by its fluid nature,
315 MHD models have difficulty accurately simulating the physics in regions where details of
316 the plasma distribution function are important, such as areas where kinetic effects are
317 dominant. As we are focussing on the magnetosheath emission this is less of an issue than
318 if we were to be looking at the cusp regions.

319
320 The Hodges neutral hydrogen model has been used in this study. A comparison of other
321 neutral hydrogen models was performed for equinox and solstice at high and low $F_{10.7}$
322 values, included as supplementary material to this manuscript. The first compared model
323 was the Bonn model [*Nass et al.*, 2006] using the coefficients from the TWINS-1 LAD data
324 [*Bailey and Gruntman*, 2011]. We also compared the *Østgaard et al.* [2003] IMAGE model;
325 while only designed to be used on the nightside, the returned values are comparable to
326 the Hodges model. The last comparison was a simple r^{-3} model with a 25 cm^{-3} number
327 density at a distance of $10 R_E$ [*Cravens et al.*, 2001]. The results of each comparison show

328 very minor differences in shape and magnitude, certainly not enough for the Hodges model
329 to be the cause of the variations between the modeled and observed lightcurves. It should
330 also be noted that when comparing SWCX through different parts of the magnetosheath,
331 *Kuntz and Snowden* [2008] demonstrate that the solar wind flux is a more important
332 factor than the magnetosheath density along the line of sight. This indicates that small
333 differences in the Hodges number density are unlikely to make any significant differences.

334

335 We next investigate the mask used to remove the cold terrestrial plasma. The Shue model
336 is a commonly used magnetopause positional model [e.g. *Liemohn et al.*, 1999; *Dimmock*
337 *et al.*, 2015] providing a subsolar distance and flaring value based on solar wind conditions.
338 The position of the magnetopause has been extensively tested with our model output. In
339 terms of subsolar stand off distance, the position appears reasonable most of the time
340 but as the model has no historical knowledge of the conditions it can change position
341 rapidly while the plasma simulation suggests a slower movement. This swift movement
342 results in the mask occasionally being placed within the plasmasphere as described by
343 the GUMICS-4 model, allowing the dense terrestrial plasma to be included in the X-ray
344 emission grid increasing the integral line emission by several orders of magnitude as seen
345 in the modeled emission in Figure 2a). It is apparent these large magnitude increases
346 are due to poor masking by looking at the normalized data of case 01-1, panel j) of
347 Figure 2. In this normalisation panel we have included emission along the x -axis without
348 any masking in red, by providing no mask we can determine whether large increases are
349 due to higher emission or errors in mask position. At 12:00UT in panel j) we see a very
350 large increase in integral magnitude, yet there is only a small increase in the non-masked

351 subsolar emissivity. At this time B_z turns negative which will instantly move the Shue
352 mask position Earthward, while the MHD model will take time for this change to have
353 an effect. *Gordeev et al.* [2013] generally found good agreement between the empirical
354 Shue magnetopause and the fluopause [*Palmroth et al.*, 2003] defined from GUMICS-4
355 simulations. The greatest differences were found in strong southward B_z conditions near
356 the subsolar point, where the simulated magnetopause position can be up to 15-20% more
357 distant than the Shue model. This masking issue is also discussed more fully in *Kuntz*
358 *et al.* [2015] who use a closed field line model to place the mask on their BATS-R-US
359 MHD model [*Powell et al.*, 1999]. The closed field line approach was not used in this
360 study as the field model will respond in a similar instantaneous movement to the Shue
361 magnetopause model, resulting in similar errors.

362

363 An MHD model based magnetopause has been trialed for our case studies, constructed
364 by applying a gaussian fit to the proton number density along the sub-solar line. The
365 magnetopause can then be taken as a full width half maximum distance from the central
366 location, an example is shown in panel k) of Figure 2 as the black dashed line. The
367 positional difference between the Shue and proton defined boundaries is small but the
368 proton boundary is much smoother. This model defined magnetopause produces excellent
369 subsolar distances as defined, but with no angular data the magnetospheric flanks are
370 poorly determined. During the testing process we also attempted a region threshold
371 detection method, which failed regularly due to the low intensity of the flanks compared
372 to the nose. As it is clear where the Shue method differs from the MHD model (by the
373 dramatic increase in integral emission), it is simple to remove these times by applying a

374 magnitude upper limit of 10 counts per second to the model count rate data.

375

376 This leaves only the alpha value as the main source of variation error. While the cross
377 sectional data for all possible solar wind ions in the 0.5 - 0.7 keV range is limited, it is
378 assumed that O^{7+} and O^{8+} are the major contributors and other ion species line spectra
379 in this range will be negligible. Hence, we are left with the upstream data inputs on the
380 oxygen charge state abundance and total oxygen number density. These values are highly
381 variable over each case and so we investigate whether the variance in oxygen data from
382 ACE is responsible for the primary variation in the simulated X-ray emission.

4.2. Oxygen composition data

383 Previously utilised empirical models have been run using constant values for the oxygen
384 to hydrogen ratio and the charge state abundances. Whilst these values have been used as
385 a back up for missing compositional data bins during the analysis process, the variability
386 from the ACE data to the constant values has been quite high. This in turn could be a
387 source of error either in the observed oxygen data or for models using the constant values.
388 As part of this study we have included not only the nineteen cases with data analysed in
389 the results section, but also the five cases where the XMM-Newton pointing direction did
390 not intersect the datacube. These extra cases are labelled in Table 1.

391

4.2.1. Oxygen to hydrogen ratio

393 The model constant values of the oxygen to hydrogen ratio (O/H) are 6.45×10^{-4}
394 for fast solar wind and 5.62×10^{-4} for slow solar wind [*Schwadron and Cravens, 2000*].
395 Investigating the data values given by ACE, suitably time delayed to the bow shock, we

396 note some wide variation from these constant values. Across all 24 cases the median and
397 mean O/H ratios are 3.11×10^{-4} and 3.94×10^{-4} respectively with a standard deviation
398 of 3.01×10^{-4} . While there is likely to be a reasonable amount of error in the ACE data
399 values due to limited instrument sensitivity, viewing angle and resolution, this should still
400 produce an average value close to the Schwadron and Craven (hereafter referred to as
401 S&C) constant values if both are representative.

402
403 Panel a) of Figure 5 shows the O/H ratio across all 24 case studies in date order, with
404 each data point taken at a 300s resolution. The solid orange background shows the extent
405 of the mean value for each case ± 1 standard deviation. The solid blue line within each
406 region shows the mean value, while the data are shown in black. The S&C values of the
407 O/H ratio are indicated by the dashed red and blue lines for fast and slow solar wind
408 respectively. This plot is complemented by a histogram of the ratio distribution in panel
409 b) with a bin size of 5×10^{-5} . This histogram shows a skewed normal distribution, with
410 the S&C constant values intersecting at a ratio greater than the FWHM value.

411
412 When we compare the O/H ratio to solar wind speed, using a 500 km/s cutoff between
413 fast and slow solar wind, the fast solar wind shows a correlation between speed and ratio.
414 We also observe that a comparison of the O/H ratio to the solar wind proton density
415 shows a correlation, indicating that the dynamic pressure should provide a correlation too
416 (as it is based on speed and density). While the speed and density plots are not included
417 for space, we have plotted the O/H ratio against the solar wind dynamic pressure in panel
418 c) of Figure 5 with the slow solar wind data points in black (dashed red fit line) and the

419 fast solar wind ratio values in blue (solid red fit line). We observe that as expected, the
 420 fast solar wind correlates very well ($r^2 = 0.78$), producing the power law fit shown below.

$$421 \quad \frac{O}{H} = 6.42 \times 10^{-4} P_{dyn}^{-3.19} \quad (3)$$

422
 423 The slow wind fit correlates poorly ($r^2 = 0.21$) which is an expected result from the lack
 424 of correlation with both speed and density. The dynamic pressure relation could simply
 425 be symptomatic of the ACE measurements increasing in signal to noise ratio as the total
 426 solar wind content increases, producing more accurate results. It should be noted that a
 427 constant ratio value defined by the median of the slow wind data ($\sim 3.17 \times 10^{-4}$) is more
 428 appropriate in these cases than using the S&C value of 5.62×10^{-4} .

430 4.2.2. Oxygen charge state ratios

431 The other data observations required in the α value determination are the O^{7+} and
 432 O^{8+} abundances as a fraction of the total solar wind oxygen. The values taken from
 433 Table 1 of *Schwadron and Cravens* [2000] give abundances of 0.2 and 0.07 for O^{7+} and
 434 O^{8+} respectively for the solar wind. These slow wind values are used as a replacement
 435 for missing observational data for all cases. The S&C abundance values for fast wind
 436 are 0.03 and 0.00 for O^{7+} and O^{8+} , indicating that only 3% of the oxygen is available
 437 to produce SWCX in the 0.5 to 0.7 energy range. Using these values are likely to result
 438 in undetectable count rates, which from Figures 3 and 4, is clearly not the case and so
 439 the slow wind abundances are used for fast wind cases as well. Figure 5 shows the mean
 440 abundance taken from ACE of O^{7+} (panel d) and O^{8+} (panel e) for each of the 24 cases
 441 with the expected value shown as the red dashed line. As the abundance values are given

442 on a 2 hour resolution most cases have fewer than 5 measurements and so a standard
 443 deviation is not appropriate for visualising the variance of the charge states. The error
 444 bars on the plots in panels d) and e) show the maximum and minimum values in each case.
 445 We note that looking at panel d), 14 of the 24 O^{7+} cases (58%) have error bars that do
 446 not cross the expected value at all. The O^{8+} abundance ranges show a similar result with
 447 13 of 24 cases (54%) where the error bars do not cross the equivalent expected value. The
 448 mean and median values for all O^{7+} cases are 0.28 and 0.31, while the equivalent averages
 449 for O^{8+} are 0.05 and 0.03. The mean values suggest the S&C constant abundance value
 450 is acceptable for both charge states, however, this does not take into account the high
 451 variability. The final panel (panel f) of Figure 5 shows the O^{7+} to O^{8+} abundances, with
 452 the red dashed lines showing the appropriate expected values. The correlation between
 453 O^{7+} and O^{8+} abundance is to be expected and we can fit a power law to the data (shown
 454 in blue), given by $O^{7+} = 0.78 O^{8+ 0.32}$.

455
 456 It should be noted that during our analysis we noticed that in certain cases the O^{8+}
 457 abundance value from ACE reached exceptionally high values. Therefore one of the
 458 conditions put in place during our analysis was that the O^{8+} abundance was not allowed
 459 to exceed 0.2, any values which did were set to the *Schwadron and Cravens* [2000] value
 460 of 0.07. This limit was an arbitrary value based on the expected O^{7+} abundance and was
 461 only enforced due to a few exceptionally high abundances causing non-physical variances
 462 in the GUMICS-4 simulated count rate. Three cases required this adjustment to one of
 463 the O^{8+} data points; 02-3, 03-4, and 03-6. The relation between O^{7+} and O^{8+} abundances
 464 in panel f) of Figure 5 suggests the O^{8+} abundance at ~ 0.15 may also be artificially high.

465 The same is true for the O^{7+} abundance at ~ 0.52 , without a reference for the range of
 466 values that this abundance can take we did not limit the O^{7+} value in this study.

5. Reanalysis with a constant O/H ratio

5.1. Removing the oxygen variation

467 We have observed from the rapid changes in oxygen composition and number density,
 468 that the oxygen variances observed in each case are high. To attempt to determine if
 469 the oxygen variance is causing strong model emission variances we have reanalysed two
 470 case studies with a range of O/H and charge state abundance values. The important
 471 difference is that we do not allow the oxygen values to vary over the cases. The two
 472 cases (00-2 and 01-3) were chosen because of their difference from the modal oxygen value
 473 in Figure 5. Case 01-3 is also the observation used in *Carter et al.* [2010] for observing
 474 SWCX enhancement during a coronal mass ejection interaction with the magnetosheath.
 475 Figure 6 shows the two cases with 00-2 in the left panels and 01-3 in the right panels. The
 476 top row shows the original model result using ACE oxygen composition data, the blue line
 477 shows the model counts and the black line is the observational data points included with
 478 the appropriate errorbars. The second row of Figure 6 shows the *Schwadron and Cravens*
 479 [2000] O/H ratio of $\frac{1}{1780}$ for slow solar wind and O^{7+} and O^{8+} abundances of 0.2 and 0.07
 480 applied respectively. The third row of Figure 6 shows the results from using the modal
 481 O/H ratio from Figure 5 of 2×10^{-4} and using the case mean O^{7+} and O^{8+} abundances.
 482 The final row of Figure 6 shows the results from using the mean O/H ratio, O^{7+} , and
 483 O^{8+} abundances from each case. These mean values for case 00-2 are 7.26×10^{-4} for the
 484 O/H ratio, 0.19 for the O^{7+} abundance and 0.027 for the O^{8+} abundance. The equivalent
 485 values for case 01-3 are 5.03×10^{-5} for the O/H ratio, 0.31 for the O^{7+} abundance and

486 0.14 for the O^{8+} abundance.

487

488 Figure 6 clearly shows that in both cases setting the O/H ratio to a constant results
489 in a simulated lightcurve variance that is a lot closer to that of the observed variance.
490 The magnitude of the ratio can be seen to directly affect the magnitude of the output
491 X-ray emission. In terms of matching the magnitudes as closely as possible, the modal
492 O/H ratio from Figure 5 provides the closest match for both examples in Figure 6. We
493 therefore recalculate all our simulated X-ray emission lightcurves using a constant O/H
494 ratio of 2×10^{-4} and the mean O^{7+} and O^{8+} abundances for each case. Each case
495 comparison is shown once again in Figures 7 and 8, which can be directly compared to
496 Figures 3 and 4.

5.2. Accuracy of the modeled to observed magnitudes

497 A comparison of the cases with a fixed O/H ratio and those using ACE in Figures 3,
498 4, 7 and 8 allows an initial quality check by eye. Of the 19 cases, 11 show visible
499 improvement (58%), 5 show little to no improvement (26%), and only 3 cases show a
500 decline in both magnitude and variance matching (16%). This basic check confirms that
501 we should continue the analysis with these new simulations.

502

503 Figure 9 shows the comparison of these newly calculated model count rates to the
504 background removed EPIC observations. The top panel shows both the mean and median
505 magnitude ratio between the modeled and observed counts for each case. Taking the
506 median ratios, the minimum value is 0.38, the maximum is 12.45 and the median value is
507 2.23. This range shows that while the median magnitude is slightly higher in ratio than

508 the ACE varying modeled count rates, the range of the spread is much smaller. This
509 can be seen by the fact that 8 of the 19 case averages (42%) now sit within a factor of
510 2 higher or lower of the observation magnitude average, two cases greater than the ACE
511 O/H varying results (Section 3.2). The second panel of Figure 9 shows the correlation
512 value of the modeled and observed count rates. In comparison to the ACE varying data,
513 the median correlation is now 0.35 (compared to 0.07) with a standard deviation of 0.48
514 (compared to 0.52) and 5 of the cases show negative correlation. This indicates that by
515 removing the oxygen variation we obtain much better correlations between the model and
516 observations. The median of the absolute value of correlation is 0.57 (compared to 0.44),
517 indicating that whether the case is positively or negatively correlated the variances are
518 more closely related with the O/H ratio kept constant.

519

520 The lower panel of Figure 9 shows a scatter plot of each observed count rate bin against
521 the respective modeled count rate for all cases. The scatter plot is accompanied by
522 histograms of each count rate distribution. The solid black line indicates an exact count
523 rate match between observation and modeled count rates and, as expected by the case
524 average magnitude ratio of 2.23, most of the data points sit above this line. This is
525 illustrated further by the red dashed lines which indicate the modal count rate bins, the
526 EPIC modal value of 0.087 counts is approximately half the modal GUMICS-4 count
527 rate of 0.199. This approximate factor of two is duplicated in the median of all data
528 points (blue dashed line) where the EPIC value is 0.091 compared to the GUMICS-4
529 median value of 0.218. The actual factor of 2.4 is slightly different from the case average
530 value of 2.23 due to the fact that each observation ranges in length from 3 hours to 26.5

531 hours. It should be noted that the histogram of varying O/H modeled count rates (not
532 shown) resulted in a bi-modal distribution at 0.16 and 0.63 counts per second which is
533 not repeated when the O/H ratio is kept constant.

5.3. Comparing SWCX quiet and enhanced times

534 As well as looking at the correlation value we can also compare the model and observed
535 count rates to ensure that both are seeing more generalised X-ray emission enhancement
536 at the same time. We determine the periods of enhancement during each case from the
537 observed count rate lightcurve, given in *Carter et al.* [2011]. Each case shows a definitive
538 period of enhancement which can be either from the start of the observation, near the
539 end of the observation or sometime between the start and end. By determining these
540 enhancement cut off times we separate out the observed and model count rates for each
541 case into quiet and enhanced categories. Taking the mean count rate of both the quiet
542 and enhanced periods, we can create both a ratio and difference value between the two
543 for each case.

544

545 Figure 10 shows the values for the ratio between enhanced to quiet count rate. The top
546 panel shows the cases in data order with each symbol representing; the EPIC observed
547 ratio (green circle), the modeled ratio with an ACE varying O/H value (black star), and
548 the modeled ratio with a constant O/H value (red plus). Placing all the case values in date
549 order shows there are no temporal trends such as a decrease in accuracy with solar cycle or
550 instrument degradation. The dashed line shows the 1:1 ratio with any points falling below
551 the line indicating that the enhanced time is producing less flux. By definition, the EPIC
552 observations all fall above the ratio line with a mean increase of 48% and median increase

553 of 22% in c/s during SWCX enhancement times. The O/H varying cases have four cases
554 where the ratio is less than 1, indicating that the SWCX enhanced period is returning less
555 X-ray emission. Whereas, for the constant O/H there are only two cases where this occurs.
556 The mean and median count rate increases for the O/H varying model are 370% and
557 53% respectively. The equivalent values for the constant O/H model are 116% and 96%
558 respectively. While the varying O/H data provides a median increase between quiet and
559 enhanced times similar to that seen in the observed data, the extremely high mean value
560 indicates this is subject to high variation. The constant O/H ratio enhancement again
561 shows a factor of two in both the mean and median enhancement rates. We investigate
562 this further by plotting out each modeled enhancement ratio against the observed values
563 in the lower two panels of Figure 10. The left panel shows the ACE varying enhancement
564 ratio and the right panel shows the constant O/H enhancement ratio values, to be able
565 to show both data sets on the same scale we have plotted these on a log x axis. The solid
566 red line indicates the $y=x$ line for ease of comparison. The variability of the results can
567 once again be seen in the ACE varying model data although around the ratio of 1.5 the
568 observations match up to the model extremely well. The constant O/H enhanced ratio
569 values show a tighter spread but a reduced accuracy in the cases which matched well in
570 the varying O/H plot.

571

572 The ratio between enhanced and quiet times will be very sensitive to the quiet time
573 magnitudes, which in turn will be heavily influenced by the calculated background values.
574 As a complement to the ratio calculation we have also determined the magnitude difference
575 between enhanced and quiet times for each case, shown in Figure 11. The top panel

576 shows the difference values in time order, again showing no temporal pattern between
577 observations and model results. The mean and median enhancements are 0.08 and 0.06
578 counts per second for the observed differences, 0.05 and 0.04 for the ACE varying model,
579 and 0.15 and 0.09 for the constant O/H model. The lower panels of Figure 11 show the
580 scatter plot between observed and model differences, the solid red line in each plot shows
581 the line of unity. The lower left plot also indicates the position of an outlying point at a
582 model difference value of -0.63 c/s, this has been shown in blue. The ACE varying data
583 shows a similar result to Figure 10 with a few cases correlating very well to the observed
584 differences but the spread is wider than the constant O/H model data. The data from
585 both the difference and ratio between enhanced and quiet times agrees, in some cases the
586 ACE varying data does an excellent job while setting the O/H ratio to constant produces
587 a more reliable result but reduces accuracy.

588

589 The case of April 17 2002 (02-2) has no enhanced to quiet ratio for either O/H value
590 as the enhancement occurs in the final two bins of the observation and neither simulation
591 returns counts for this period.

5.4. Positional accuracy

592 As a final piece of analysis we have also displayed the spatial position of the model data
593 using a constant O/H ratio in Figure 12. The left panel shows the data in a cylindrical
594 coordinate system ($x-r$) with the r axis signed by whether the y value is positive or
595 negative. This view gives us positional values projected onto a 2D plane with a $0.5 R_E$ by
596 $1 R_E$ resolution. We have binned all the data points and taken the average integral count
597 rate for each bin, with our limited number of case studies this leaves a large proportion

598 of the grid without any data but does show that the higher modeled count rates occur
599 when the satellite is looking in the positive y direction (dusk). The top right panel of
600 Figure 12 shows the data binned in the y - z plane, with no dependence upon the x value.
601 We can again observe the asymmetry in y but the highest count rates occur at the z values
602 closest to zero, as these values are likely to be closest to the nose of the magnetosheath it
603 could simply be a proximity relation to the highest emission rates. To determine whether
604 distance from the magnetopause is significant we plot each model count rate against the
605 radial distance from the Shue magnetopause during the specific data point conditions.
606 This scatter plot is shown in the middle right panel of Figure 12, with the data points
607 split by y position. The positive y values are shown by black + signs and the negative y
608 values are shown by blue * symbols. When looking at all the data points combined we
609 can see that the count rate increases with distance from the magnetopause. This result
610 is initially counterintuitive as we would expect the count rate to be higher the deeper in
611 the magnetosheath the satellite is. What must be considered is the pointing direction
612 and case selection bias. A case where the satellite is far from the magnetopause would
613 only have shown initial significant SWCX if the pointing direction intersected a significant
614 fraction of the magnetosheath. As the satellite comes closer to the Earth the integral path
615 through the data grid includes fewer bins. If we took a sample of spacecraft positions with
616 the spacecraft pointing in random directions then the opposite relation should be true.
617 This magnitude plot shows, in a similar manner to the binned grid plots, that the count
618 rates when y is positive are generally higher. The final plot of Figure 12, in the lower
619 right panel, shows average distance from the magnetopause with correlation between the
620 observed and modeled lightcurves. These data points are again split by whether y is

621 positive or negative. There appears to be no general pattern between lightcurve variance
622 and magnetopause distance, although the highest correlations occur in the negative y
623 value (dawn) data values. This asymmetry was also mentioned in *Carter et al.* [2011],
624 where they found that the empirical model fitted better in the dawnside. This dawn-
625 dusk asymmetry could be related to the known asymmetries in either the magnetosheath
626 plasma conditions [e.g. *Walsh et al.*, 2012] or magnetopause position [e.g. *Dmitriev et al.*,
627 2004], indicating that this asymmetry needs to be considered during the modeling process.

628

6. Conclusions

629 In this study we have taken the data from 19 case studies using the EPIC-MOS
630 instruments on XMM-Newton to examine the accuracy of MHD modeling when describing
631 solar wind charge exchange from the Earth's magnetosheath. We found that a large
632 amount of variation in the modeled lightcurve was caused by variations in the oxygen
633 to hydrogen ratio and abundances of oxygen charge states. In a large number of these
634 cases setting the oxygen to hydrogen ratio to a constant improved the variance matching.
635 These modeled data values with a constant O/H ratio and mean charge state abundances
636 were then compared to the observed lightcurves, providing an average correlation value
637 of 0.35. This correlation has been reduced by the fact that five of the nineteen cases are
638 anti-correlated. The average magnitude ratio is a factor of 2.4 when averaging across all
639 data points, giving 42% of the cases having an average magnitude within a factor of two
640 of the observed data values, a slight decrease on the empirical method used in *Carter*
641 *et al.* [2011]. The highest modeled count rates occur when the satellite is in the positive
642 GSE y , with the highest correlations arising in negative y (dawn).

643

644 It is clear from Sections 4.2 and 5 that the oxygen data inputs to the MHD model include
645 substantial errors. The O/H variances cause large changes in the modeled lightcurves
646 which are simply not seen in the observed lightcurves for a significant number of cases. The
647 longer (temporally) the case is, the more likely that a constant O/H ratio is inappropriate,
648 yet accurate data is needed. The same applies to the oxygen charge state abundances, the
649 two hour resolution of this data is low for modeling that runs at a four second calculation
650 resolution and a five minute grid output. The absolute abundance values themselves are
651 also an issue, it is unknown what the upper and lower limits of O^{7+} and O^{8+} should be.
652 We observed in Figure 5 that the O^{7+} abundance can take a wide range of values, up
653 to 52% which is likely unphysical. It is certain that the values given in *Schwadron and*
654 *Cravens* [2000], while of the right order of magnitude, are of limited use for this particular
655 modeling, especially as they describe almost no highly charged states in the fast wind.
656 To improve on model accuracy we either require more accurate and numerous solar wind
657 oxygen observations closer to the Earth, or an accurate proxy such as an extension of
658 the proton entropy correlation work by *Pagel et al.* [2004] to include the O^{8+}/O^{7+} ratio.
659 Using a constant value for the O/H ratio of 2×10^{-4} , and mean oxygen charge states for
660 each case we have removed a large amount of this variation at the cost of a small accuracy
661 loss (e.g., Figures 10 and 11).

662

663 The accuracy of the MHD modeling ranges from anti-correlated to an excellent correlation.
664 We can link several of the errors in both magnitude and variance to the oxygen data, and
665 the disparity of the MHD magnetopause position to the Shue model. The other data

666 inputs to the MHD model behave well and we have some excellent comparisons as seen in
667 Figures 7 and 8. When comparing the MHD model to the empirical model used in *Carter*
668 *et al.* [2011] we can say that it performs equally well. The slight decrease of magnitude
669 matching, 42% rather than 50%, of cases within a factor of two, could easily be due to
670 the background removal. Decreasing the background removal values by 0.03 c/s actually
671 increases the magnitude comparison accuracy to 63%, hence showing the importance of
672 the background removal when we look at comparing the magnitudes. The background
673 removal does not affect the correlation or the enhanced to quiet differencing comparison
674 however. Examining the magnitude difference between quiet and enhanced periods, we
675 see very similar results between the observed values and the MHD model. The difference
676 in the dawn-dusk correlations, also seen in *Carter et al.* [2011], suggests that there could
677 be an asymmetrical process affecting the charge exchange emission magnitude, which is
678 missing from both models.

679
680 Users wishing to estimate the near-Earth SWCX values are advised that using either
681 the empirical model or an MHD model with constant solar wind oxygen parameters are
682 equally likely to produce a useable value. When comparing enhanced to quiet times, i.e.,
683 taking an average over a longer time period, using the variable O/H data is likely to be
684 a valid approach. For those interested in a more in depth view of what is happening in
685 terms of global SWCX around the Earth, the MHD based model with a constant oxygen
686 ratio and abundances, will produce a more accurate result, including matching short time
687 scale emissivity variation. This study also acts as a validation of the model methodology
688 for global imaging of the magnetosheath using SWCX, by providing similar emissivities

689 to observed values. However, the relative inaccuracy of using a far upstream monitor for
690 the solar wind conditions can affect the model results considerably. This modeling will be
691 especially important for future missions involving wide angle X-ray imaging of the Earth's
692 magnetosheath.

693 **Acknowledgments.** This research used the ALICE/SPECTRE High Performance
694 Computing Facility at the University of Leicester. The GUMICS-4 MHD code
695 is provided by the Finnish Meteorological Institute, while the simulation runs are
696 stored on the HPC facilities at the University of Leicester. The OMNI solar
697 wind data was taken from NASA's GSFC/SPDF repository (*omniweb.gsfc.nasa.gov*).
698 The ACE solar wind composition data was taken from the ACE Science Center
699 *www.srl.caltech.edu/ACE/ASC/*. The background count rates were calculated using the
700 WebPIMMS service (*heasarc.gsfc.nasa.gov/cgi-bin/Tools/w3pimms/w3pimms.pl*). Effort sponsored by
701 the Air Force Office of Scientific Research, Air Force Material Command, USAF, under
702 grant number FA9550-14-1-0200. The U.S. government is authorized to reproduce and
703 distribute reprints for Governmental purposes notwithstanding any copyright notation
704 thereon. JAC and SEM gratefully acknowledge support from the STFC consolidated
705 grant ST/K001000/1.

References

- 706 Bailey, J. and M. Gruntman. (2011), Experimental study of exospheric hydrogen atom
707 distributions by Lyman-alpha detectors on the TWINS mission, *J. Geophys. Res.*, **116**
708 A09302, doi:10.1029/2011JA016531
- 709 Bodewits, D. (2007), PhD thesis, University of Groningen, The Netherlands.

- 710 Carter, J. A., and A. M. Read (2007), The XMM-Newton EPIC background and
711 the production of background blank sky event files, *A&A*, **464**, doi:10.1051/0004-
712 6361:20065882
- 713 Carter, J. A. and S, Sembay (2008), Identifying XMM-Newton observations affected by
714 solar wind charge exchange - Part I, *A&A*, **489** 2, doi:10.1051/0004-6361/200809997
- 715 Carter, J. A., S, Sembay and A. Read (2010), A high charge state coronal mass ejection
716 seen through solar wind charge exchange emission as detected by XMM-Newton. *Mon.*
717 *Not. R. Astron. Soc.*, **402**, doi:10.1111/j.1365-2966.2009.15985.x
- 718 Carter, J. A., S, Sembay and A. Read (2011), Identifying XMM-Newton observations
719 affected by solar wind charge exchange - Part II, *A&A*, **527** A115, doi:10.1051/0004-
720 6361/201015817
- 721 Collier, M. R., T. E. Moore, M.-C. Fok, B. Pilkerton, S. Boardsen and H. Khan. (2005),
722 Low-energy neutral atom signatures of magnetopause motion in response to southward
723 Bz, *J. Geophys. Res.*, **110** A2, doi:10.1029/2004JA010626
- 724 Collier, M. R., D. G. Siebeck, T. E. Cravens, I. P. Robertson and N. Omid. (2010),
725 Astrophysics Noise: A Space Weather Signal, *Eos, Transactions American Geophysical*
726 *Union*, **91** 24, doi:10.1029/2010EO240001
- 727 Collier, M. R., F. S. Porter, D. G. Sibeck, J. A. Carter, M. P. Chiao, D. J. Chornay, T.
728 E. Cravens, M. Galeazzi, J. W. Keller, D. Koutroumpa, K. Kuntz, A. M. Read, I. P.
729 Robertson, S. Sembay, S. Snowden and N. Thomas. (2012), Prototyping a global soft
730 X-ray imaging instrument for heliophysics, planetary science, and astrophysics science,
731 *Astron. Nachr.*, **333** 4, doi:10.1002/asna.201211662

- 732 Collier, M. R., S. L. Snowden, M. Sarantos, M. Benna, J. A. Carter, T. E. Cravens, W.
733 M. Farrell, S. Fatemi, H. Kent-Hills, R. R. Hodges, M. Holmström, K. D. Kuntz, F.
734 Scott-Porter, A. Read, I. P. Robertson, S. F. Sembay, D. G. Sibeck, T. J. Stubbs, P.
735 Travnicek and B. M. Walsh. (2014), On lunar exospheric column densities and solar
736 wind access beyond the terminator from ROSAT soft X-ray observations of solar wind
737 charge exchange. *J. Geophys. Res.*, **119** 7, doi:10.1002/2014JE004628
- 738 Cravens, T. E. (1997), Comet Hyakutake X-ray source: Charge transfer of solar wind
739 heavy ions. *Geophys Res. Lett.*, **24** 105109, doi:10.1029/96GL03780
- 740 Cravens, T. E. (2000), Heliospheric X-ray emission associated with charge transfer of the
741 solar wind with interstellar neutrals. *ApJ*, **532** 2, doi:10.1086/312574
- 742 Cravens, T. E., I. P. Robertson and S. L. Snowden (2001), Temporal variations of
743 geocoronal and heliospheric X-ray emission associated with the solar wind interaction
744 with neutrals. *J. Geophys. Res.*, **106** A11, doi:10.1029/2000JA000461
- 745 Dennerl, K. (2008), X-rays from Venus observed with Chandra. *PSS*, **56** 10,
746 doi:10.1016/j.pss.2008.03.008
- 747 Dimmock, A. P., K. Nykyri, H. Karimabadi, A. Osmane, and T. I. Pulkkinen. (2015),
748 A statistical study into the spatial distribution and dawn-dusk asymmetry of dayside
749 magnetosheath ion temperatures as a function of upstream solar wind conditions, *J.*
750 *Geophys. Res.*, **120** 4, doi:10.1002/2014JA020734
- 751 Dmitriev, A. V., A. V. Suvorova, J. K. Chao and Y.-H. Yang (2004), Dawn-dusk
752 asymmetry of geosynchronous magnetopause crossings, *J. Geophys. Res.*, **109** A5,
753 doi:10.1029/2003JA010171

- 754 Geiss, J., G. Gloeckner and R. von Steiger (1999), Origin of the solar wind from
755 composition data, *Space Sci. Rev.*, **72** 49-60
- 756 Gordeev, E., G. Facskó, V. Sergeev, I. Honkonen, M. Palmroth, P. Janhunen and S. Milan.
757 (2013), Verification of the GUMICS-4 global MHD code using empirical relationships,
758 *J. Geophys. Res.*, **118** 6, doi:10.1002/jgra.50359
- 759 Henley, D. B. and R. L. Shelton (2008), Comparing Suzaku and XMM-Newton
760 Observations of the soft X-ray background: Evidence for solar wind charge exchange
761 emission. *ApJ*, **335** doi:10.1086/528924
- 762 Hodges, R. R. Jr. (1994), Monte Carlo simulation of the terrestrial hydrogen exosphere,
763 *J. Geophys. Res.*, **99** A12, doi:10.1029/94JA02183
- 764 Holmström, M., S. Barabash and E. Kallio (2001), X-ray imaging of the solar windMars
765 interaction, *GRL*, **28** 7, doi:10.1029/2000GL012381
- 766 Hosokawa, K., S. Taguchi, S. Suzuki, M. R. Collier, T. E. Moore and M. F. Thomsen.
767 (2008), Estimation of magnetopause motion from low-energy neutral atom emission, *J.*
768 *Geophys. Res.*, **113** A10, doi:10.1029/2008JA013124
- 769 Hubert, B., M. Palmroth, T. V. Laitinen, P. Janhunen, S. E. Milan, A. Grocott, S. W. H.
770 Cowley, T. Pulkkinen and J-C. Gérard. (2006), Compression of the Earth's magnetotail
771 by interplanetary shocks directly drives transient magnetic flux closure, *Geophys. Res.*
772 *Lett.*, **33** 10, doi:10.1029/2006GL026008
- 773 Ishikawa, K., Y. Ezoe, Y. Miyoshi, N. Terada, K. Mitsuda and T. Ohashi (2013),
774 Suzaku Observation of Strong Solar-Wind Charge-Exchange Emission from the
775 Terrestrial Exosphere during a Geomagnetic Storm, *Publ. Astron. Soc. Jpn.*, **65** 3,
776 doi:10.1093/pasj/65.3.63

- 777 Janhunen, P., M. Palmroth, T. Latinen, I. Honkonen, L. Juusola, G. Facskó and T. I.
778 Pulkkinen. (2012), The GUMICS-4 global MHD magnetosphere-ionosphere coupling
779 simulation, *J. Atmos. Sol. Terr. Phys.*, **80**, doi:10.1016/j.jastp.2012.03.006
- 780 Jansen, F., D. Lumb, B. Altieri, J. Clavel, M. Ehle, C. Erd, C. Gabriel, M. Guainazzi,
781 P. Gondoin, R. Much, R. Munoz, M. Santos, N. Schartel, D. Texier and G. Vacanti.
782 (2001), XMM-Newton observatory: I. The spacecraft and operations, *A&A*, **365** L1-L6,
783 doi:10.1051/0004-6361:20000036
- 784 Kalberla, P. M. W., W. B. Burton, D. Hartmann, E. M. Arnal, E. Bajaja, R. Morras and
785 W. G. L. Pöppel. (2005), The Leiden/Argentine/Bonn (LAB) Survey of Galactic HI.
786 Final data release of the combined LDS and IAR surveys with improved stray-radiation
787 corrections, *A&A*, **440** 2, doi:10.1051/0004-6361:20041864
- 788 King, J. H., and N. E. Papitashvili (2005), Solar wind spatial scales in and comparisons
789 of hourly Wind and ACE plasma and magnetic field data *J. Geophys. Res.*, **110**,
790 doi:10.1029/2004JA010649
- 791 Koutroumpa, D. (2012), Update on modeling and data analysis of heliospheric
792 solar wind charge exchange X-ray emission, *Astron. Nachr.*, **333** 341346,
793 doi:10.1002/asna.201211666
- 794 Kuntz, K. D. and S. L. Snowden (2008), The EPIC-MOS particle induced background
795 spectra *A&A*, **478** 2, doi:10.1051/0004-6361:20077912
- 796 Kuntz, K. D., Y. M. Collado-Vega, M. R. Collier, H. K. Connor, T. E. Cravens,
797 D. Koutroumpa, F. S. Porter, I. P. Robertson, D. G. Sibeck and S. L. Snowden
798 (2015), The solar wind charge-exchange production factor for hydrogen. *ApJ*, **808** 2,
799 doi:10.1088/0004-637X/808/2/143

- 800 Liemohn, M. W., J. U. Kozyra, V. K. Jordanova, G. V. Khazanov, M. F. Thomsen and
801 T. E. Cayton. (1999), Analysis of early phase ring current recovery mechanisms during
802 geomagnetic storms, *Geophys. Res. Lett.*, **26** 18, doi:10.1029/1999GL900611
- 803 Lisse, C.M., K. Dennerl, J. Englhauser, M. Harden, F. E. Marshall, M. J. Mumma, R.
804 Petre, J. P. Pye, M. J. Ricketts, J. Schmitt, J. Trümper, R. G. West (1996), Discovery
805 of X-ray and Extreme Ultraviolet Emission from Comet C/Hyakutake 1996 B2 *Science*,
806 **274** 5285, doi: 10.1126/science.274.5285.205
- 807 Milan, S. E., S. W. H. Cowley, M. Lester, D. M. Wright, J. A. Slavin, M. Fillingim,
808 C. W. Carlson, and H. J. Singer (2004), Response of the magnetotail to changes
809 in the open flux content of the magnetosphere, *J. Geophys. Res.*, **109** A04220,
810 doi:10.1029/2003JA010350
- 811 Nass, H. U., J. H. Zoennchen, G. Lay and H. J. Fahr. (2006), The TWINS-LAD mission:
812 Observations of terrestrial Lyman- α fluxes, *Astrophys. Space. Sci. Trans.*, **2** 27-31,
813 doi:10.5194/94JA02183
- 814 Ogasawara, K., V. Angelopoulos, M. A. Dayeh, S. A. Fuselier, G. Livadiotis, D. J.
815 McComas and J. P. MCFadden. (2013), Characterizing the sayside magnetosheath using
816 energetic neutral atoms: IBEX and THEMIS observations, *J. Geophys. Res.*, **118** 6,
817 doi:10.1002/jgra.50353
- 818 Østgaard, N., S. B. Mende, H. U. Frey, G. R. Gladstone and H. Lauche. (2003), Neutral
819 hydrogen density profiles derived from geocoronal imaging, *J. Geophys. Res.*, **108** A7,
820 doi:10.1029/2002JA009749
- 821 Pagel, A. C., N. U. Crooker, T. H. Zurbuchen and J. T. Gosling. (2004), Correlation
822 of solar wind entropy and oxygen ion charge state ratio, *J. Geophys. Res.*, **109** A1,

823 doi:10.1029/2003JA010010

824 Palmroth, M., I. Honkonen, A. Sandroos, Y. Kempf, S. von Alfthan and D. Pokhotelov.
825 (2013), Preliminary testing of global hybrid-Vlasov simulation: Magnetosheath and
826 cusps under northward interplanetary magnetic field. *J. Atmos. Sol. Terr. Phys.*, **99**,
827 doi:10.1016/j.jastp.2012.09.013

828 Palmroth, M., T. I. Pulkkinen, P. Janhunen and C.-C Wu. (2003), Stormtime
829 energy transfer in global MHD simulation. *J. Geophys. Res.*, **108**, A1,
830 doi:10.1029/2002JA009446

831 Powell, K. G., P. L. Roe, T. J. Linde, T. I. Gambosi and D. L. de Zeeuw. (1999), A
832 Solution-Adaptive Upwind Scheme for Ideal Magnetohydrodynamics. *J. Comp. Phys.*,
833 **154** 2, doi:10.1006/jcph.1999.6299

834 Robertson, I. P. and T. E. Cravens. (2003), Spatial maps of heliospheric and geocoronal
835 X-ray intensities due to the charge exchange of the solar wind with neutrals, *J. Geophys.*
836 *Res.*, **108** A10, doi:10.1029/2003JA009873

837 Robertson, I. P., M. R. Collier, T. E. Cravens and M.-C. Fok. (2006), X-ray emission
838 from the terrestrial magnetosheath including the cusps, *J. Geophys. Res.*, **111** A12105,
839 doi:10.1029/2006JA011672

840 Schwadron, N. A. and T. E. Cravens (2000), Implications of solar wind composition for
841 cometary X-rays, *ApJ*, **554** 558:566

842 Shue, J. H., P. Song, C. T. Russell, J. T. Steinberg, J. K. Chao, G. Zastenker,
843 O. L. Vaisberg, S. Kokubun, H. J. Singer, T. R. Detman and H. Kawano (1998),
844 Magnetopause location under extreme solar wind conditions, *J. Geophys. Res.*, **103**
845 A8, doi:10.1029/98JA01103

- 846 Slavin, J. D., B. J. Wargelin and D. Koutroumpa (2013), Solar wind charge exchange
847 emission in the Chandra deep field north, *ApJ*, **779** 1, doi:10.1088/0004-637X/779/1/13
- 848 Snowden, S. L., M. R. Collier and K. D. Kuntz (2004), XMM-Newton Observation of
849 Solar Wind Charge Exchange Emission, *ApJ*, **610** 2 1182-1190, doi:10.1086/421841
- 850 Spreiter, J. R., A. L. Summers and A. Y. Alksne (1966), Hydromagnetic flow around the
851 magnetosphere, *PSS*, **14** 223, doi:10.1016/0032-0633(66)90124-3
- 852 Strüder, L., U. Briel, K. Dennerl, R. Hartmann, E. Kendziorra, N. Meidinger, E.
853 Pfeffermann, C. Reppin, B. Aschenbach, W. Bornemann, H. Bräuninger, W. Burkert,
854 M. Elender, M. Freyberg, F. Haberl, G. Hartner, F. Heuschmann, H. Hippmann, E.
855 Kastelic, S. Kemmer, G. Kettenring, W. Kink, N. Krause, S. Müller, A. Oppitz, W.
856 Pietsch, M. Popp, P. Predehl, A. Read, K. H. Stephan, D. Stötter, J. Trümper, P.
857 Holl, J. Kemmer, H. Soltau, R. Stötter, U. Weber, U. Weichert, C. von Zanthier, D.
858 Carathanassis, G. Lutz, R. H. Richter, P. Solc, H. Böttcher, M. Kuster, R. Staubert,
859 A. Abbey, A. Holland, M. Turner, M. Balasini, G. F. Bignami, N. La Palombara, G.
860 Villa, W. Buttler, F. Gianini, R. Lainé, D. Lumb and P. Dhez. (2001), The European
861 Photon Imaging Camera on XMM-Newton: The pn-CCD camera, *A&A*, **365** L18-L26,
862 doi:10.1051/0004-6361:20000066
- 863 Turner, M. J. L., A. Abbey, M. Arnaud, M. Balasini, M. Barbera, E. Belsole, P. J. Bennie,
864 J. P. Bernard, G. F. Bignami, M. Boer, U. Briel, I. Butler, C. Cara, C. Chabaud, R.
865 Cole, A. Collura, M. Conte, A. Cros, M. Denby, P. Dhez, G. Di Coco, J. Dowson, P.
866 Ferrando, S. Ghizzardi, F. Gianotti, C. V. Goodall, L. Gretton, R. G. Griffiths, O.
867 Hainaut, J. F. Hochedez, A. D. Holland, E. Jourdain, E. Kendziorra, A. Lagostina, R.
868 Laine, N. La Palombara, M. Lortholary, D. Lumb, P. Marty, S. Molendi, C. Pigot, E.

869 Poindron, K. A. Pounds, J. N. Reeves, C. Reppin, R. Rothenflug, P. Salvétat, J. L.
870 Sauvageot, D. Schmitt, S. Sembay, A. D. T. Short, J. Spragg, J. Stephen, L. Strüder,
871 A. Tiengo, M. Trifoglio, J. Trümper, S. Vercellone, L. Vigroux, G. Villa, M. J. Ward,
872 S. Whitehead and E. Zonca. (2001), The European Photon Imaging Camera on XMM-
873 Newton: The MOS cameras, *A&A*, **365** L27-L35, doi:10.1051/0004-6361:20000087
874 Voges, W., B. Aschenbach, T. Boller, H. Bräuninger, U. Briel, W. Burkert, K. Dennerl, J.
875 Englhauser, R. Gruber, F. Haberl, G. Hartner, G. Hasinger, M. Kürster, E. Pfeffermann,
876 W. Pietsch, P. Predehl, C. Rosso, J. H. M. M. Schmitt, J. Trümper and H. U.
877 Zimmermann (1999), The ROSAT all-sky survey bright source catalogue, *A&A*, **349** 2,
878 389-405
879 Walsh, B. M., D. G. Sibeck, Y. Wang and D. H. Fairfield (2012), Dawn-dusk asymmetries
880 in the Earth's magnetosheath, *J. Geophys. Res.*, **117** A12, doi:10.1029/2012JA018240

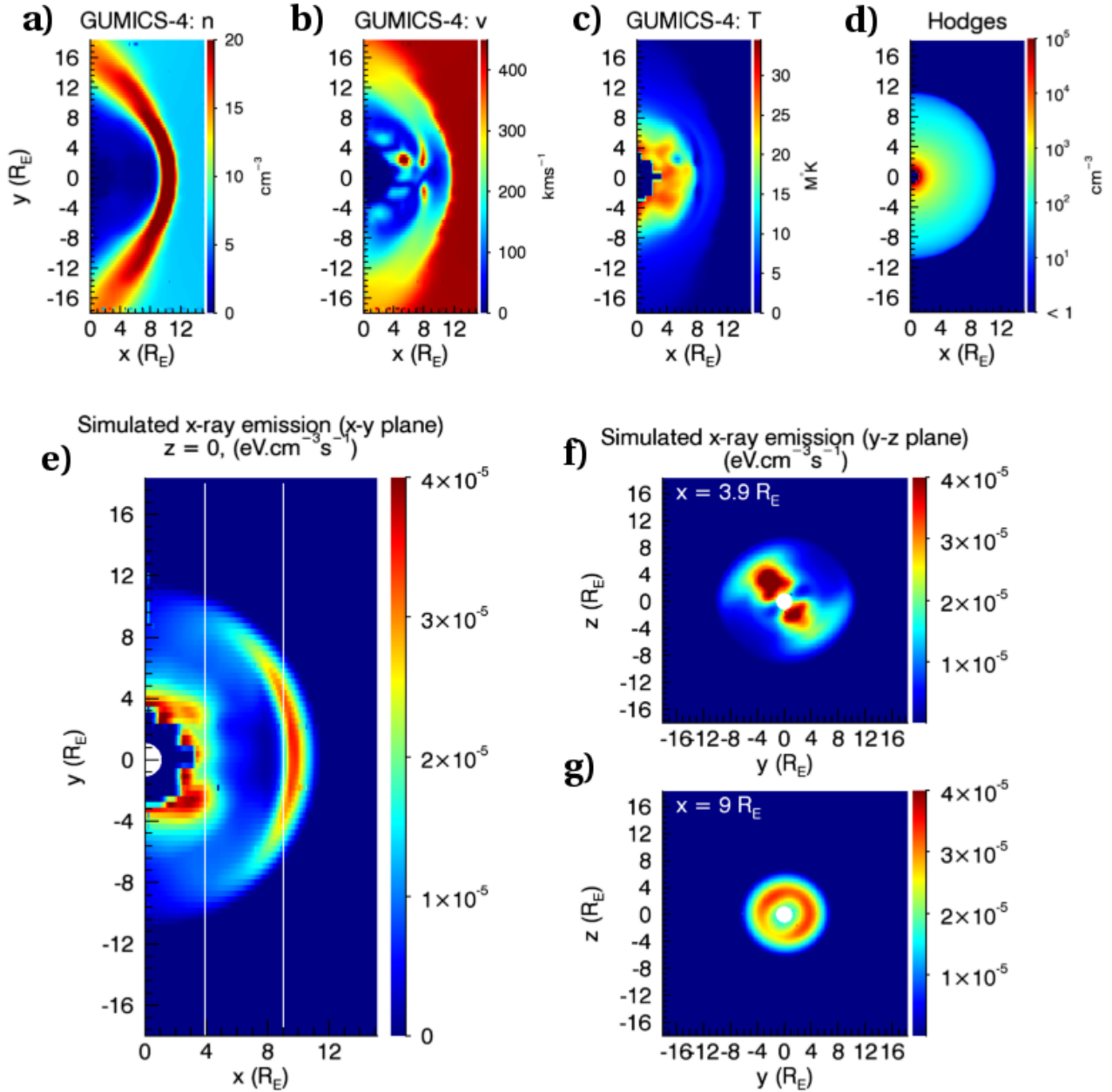


Figure 1. a) - d) The GUMICS-4 output for a single timestep showing solar wind proton number density, bulk flow speed and temperature with the final panel showing the equivalent Hodges neutral hydrogen density. Each of these panels shows a slice through the data cube in the x - y plane at $z = 0$. e) The calculated X-ray emissivity in the x - y plane, with cuts taken to show the y - z plane at $x = 3.9R_E$, the magnetopause sits around a subsolar distance of $9R_E$ and the bow shock is at approximately $11R_E$.

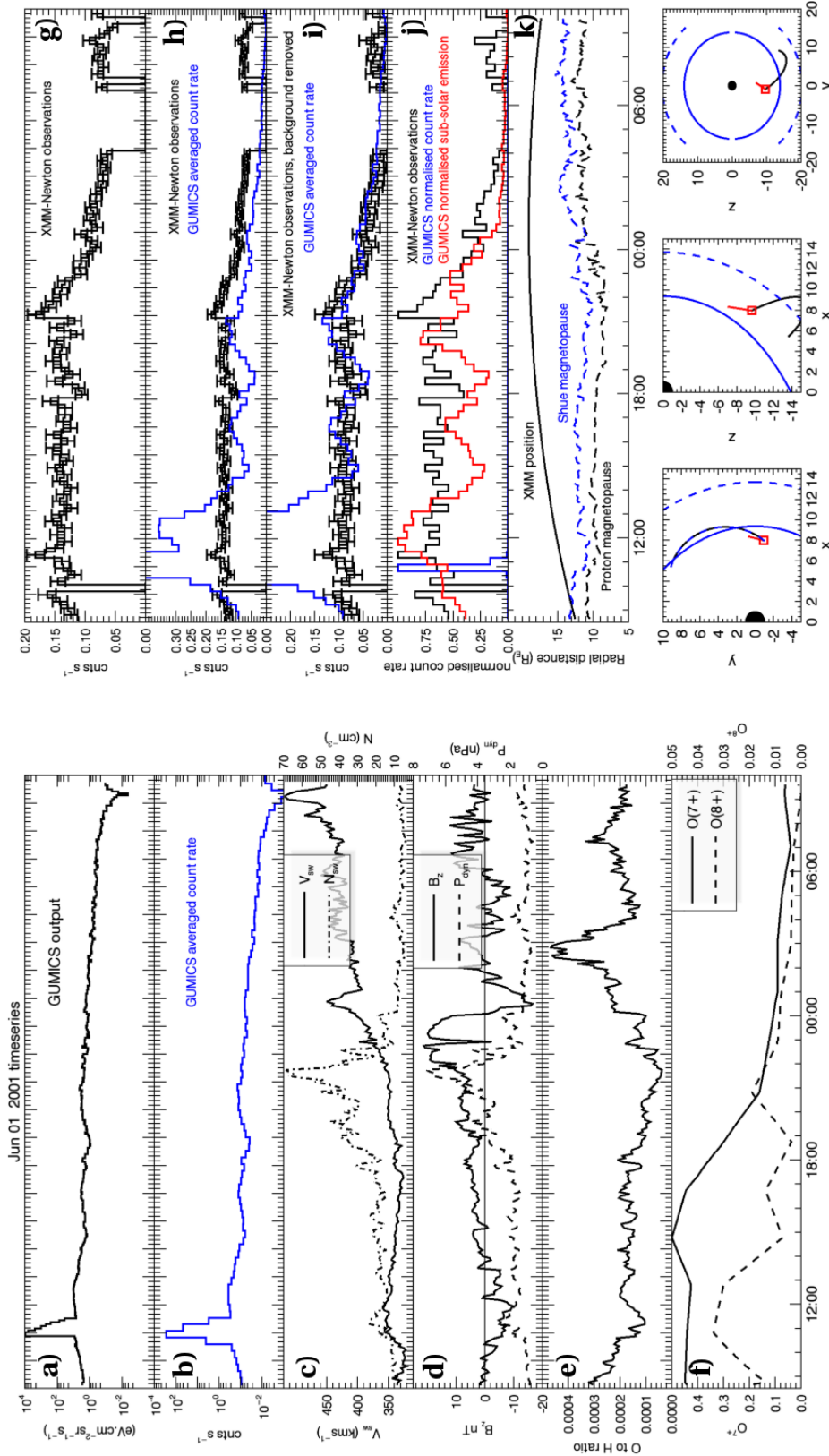


Figure 2. A set of plots showing all the specific details for an example case (01-1). The panels show; **a)** modeled X-ray integral emission, **b)** the equivalent count rates, **c)** solar wind density and speed, **d)** B_z and dynamic pressure, **e)** O/H ratio, **f)** oxygen charge state abundances, **g)** EPIC observation data, **h)** comparison of observed and modeled count rates including background, **i)** comparison of observed and modeled count rates with the background removal applied, **j)** normalized lightcurves, **k)** XMM position relative to the magnetopause, and the final panels show the orbital position.

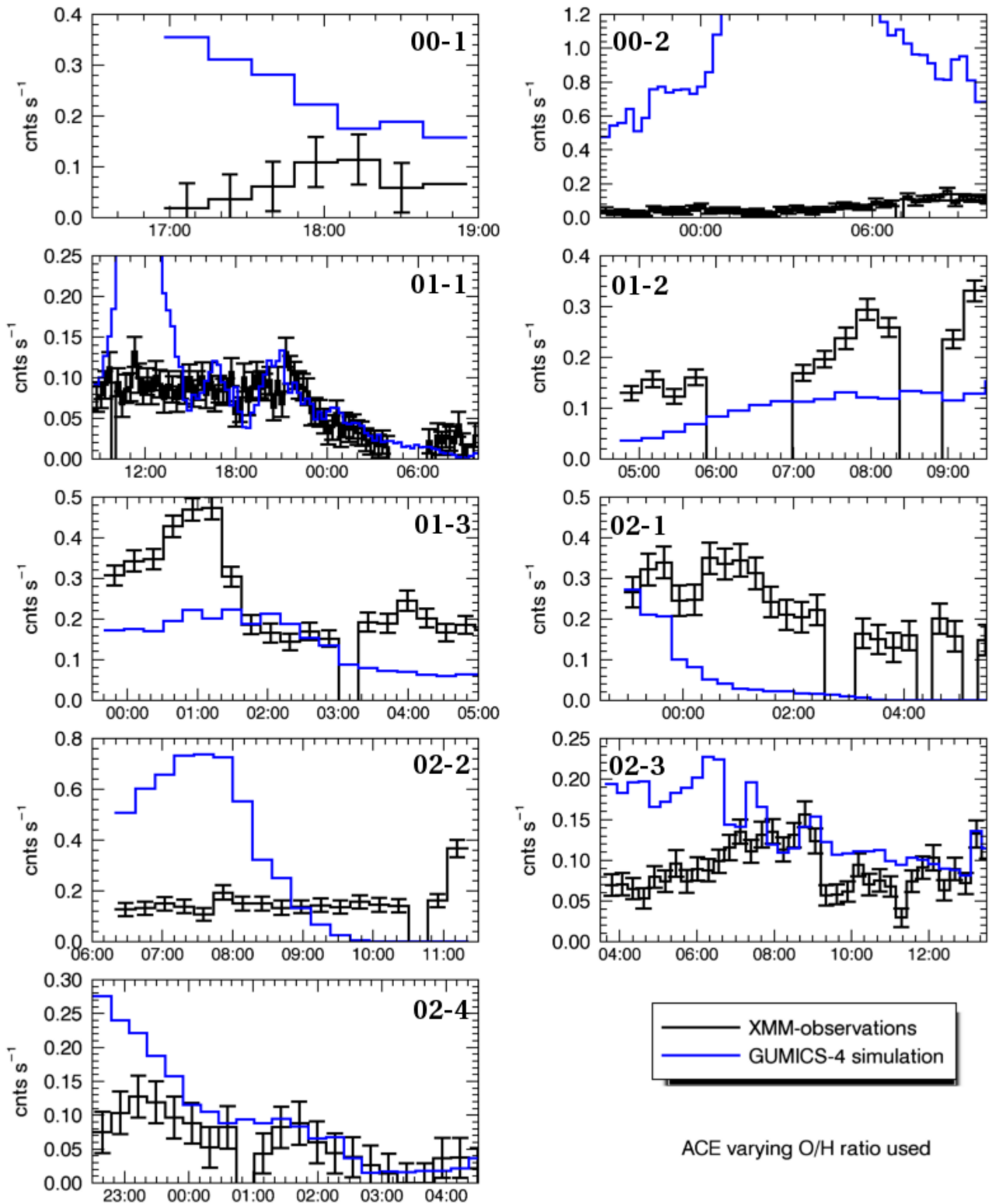


Figure 3. Cases 1-9 of the study, each panel shows the GUMCIS-4 estimated count rate in blue and the EPIC observations in black with the combined observational and background error

bars included.

D R A F T

February 12, 2016, 2:39pm

D R A F T

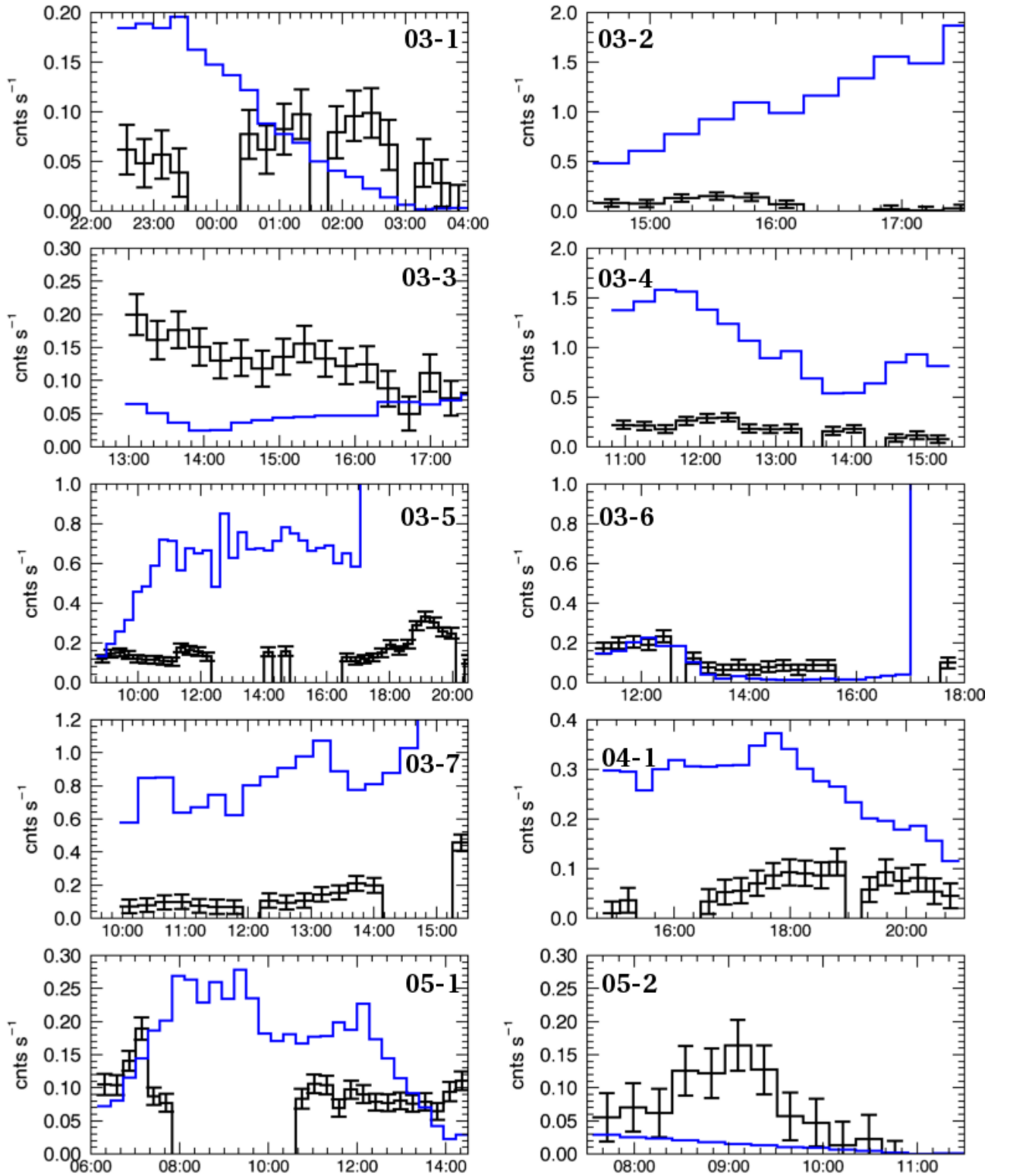


Figure 4. Cases 10-19 of the study, each panel shows the GUMCIS-4 estimated count rate in blue and the EPIC observations in black with the combined observational and background error

bars included.

D R A F T

February 12, 2016, 2:39pm

D R A F T

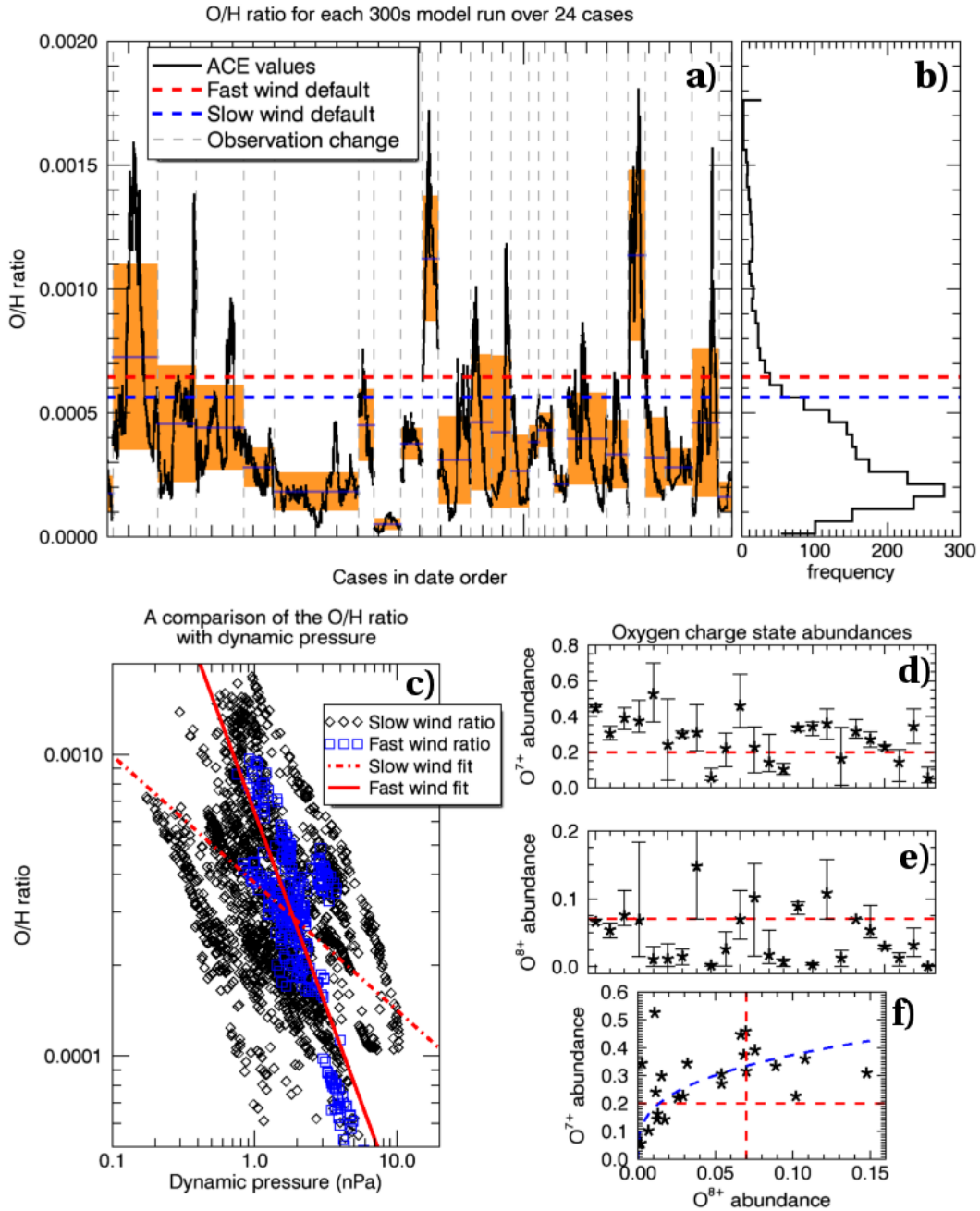


Figure 5. A selection of plots showing the variation in oxygen to hydrogen ratio and the oxygen charge state abundance. **a)** The O/H ratio for every OMNI data point used in the 24 case studies with data, **b)** the ratio in a histogram format. **c)** The slow and fast O/H ratio against solar wind dynamic pressure. **d)** and **e)** The average O⁷⁺ and O⁸⁺ charge state abundance for each case. **f)** The O⁷⁺ charge state abundance plotted against the O⁸⁺ abundance.

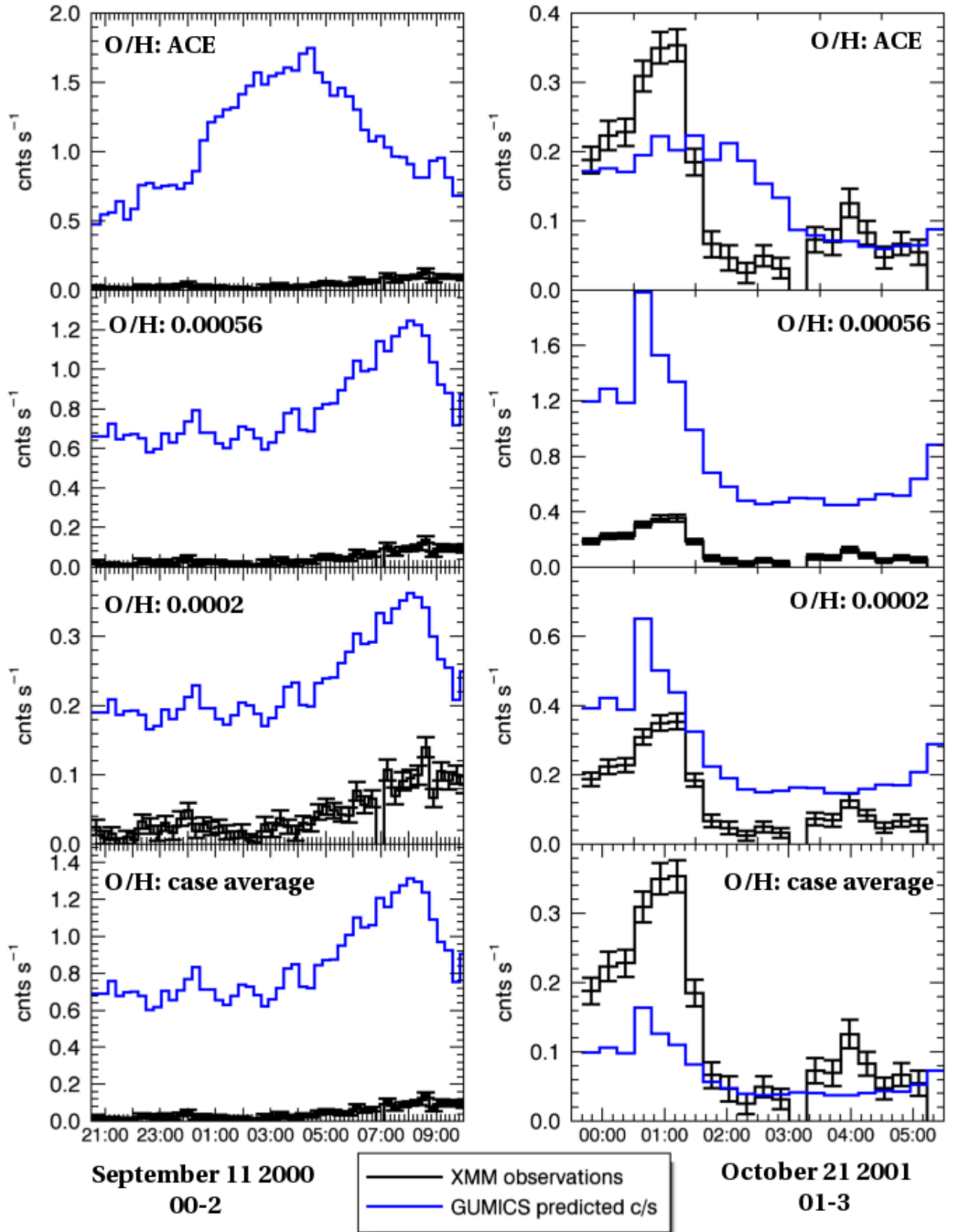


Figure 6. A comparison of changing the oxygen to hydrogen ratio. Each panel shows the XMM-

Newton observations for cases 00-2 and 01-3 (in black with errorbars) as well as the GUMICS

D R A F T

February 12, 2016, 2:39pm

D R A F T

simulation in blue. Keeping the O/H ratio constant produces a variation in the simulated light

curve closer to the observed values, in comparison to the ACE varying O/H ratio in the top

panels.

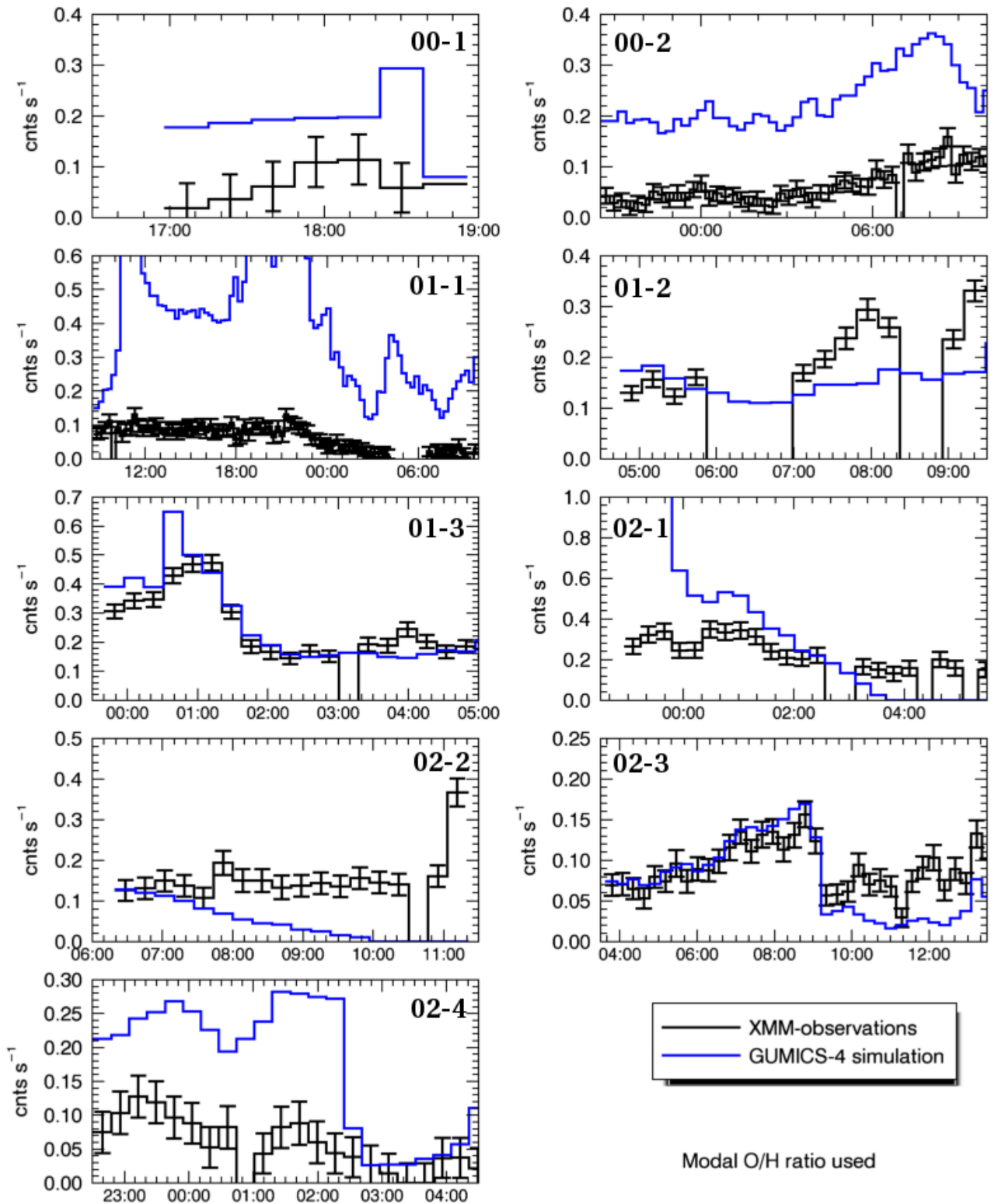


Figure 7. Cases 1-9 of the study using a constant O/H ratio, each panel shows the GUMCIS-4 estimated count rate in blue and the EPIC observations in black with the combined observational and background error bars included.

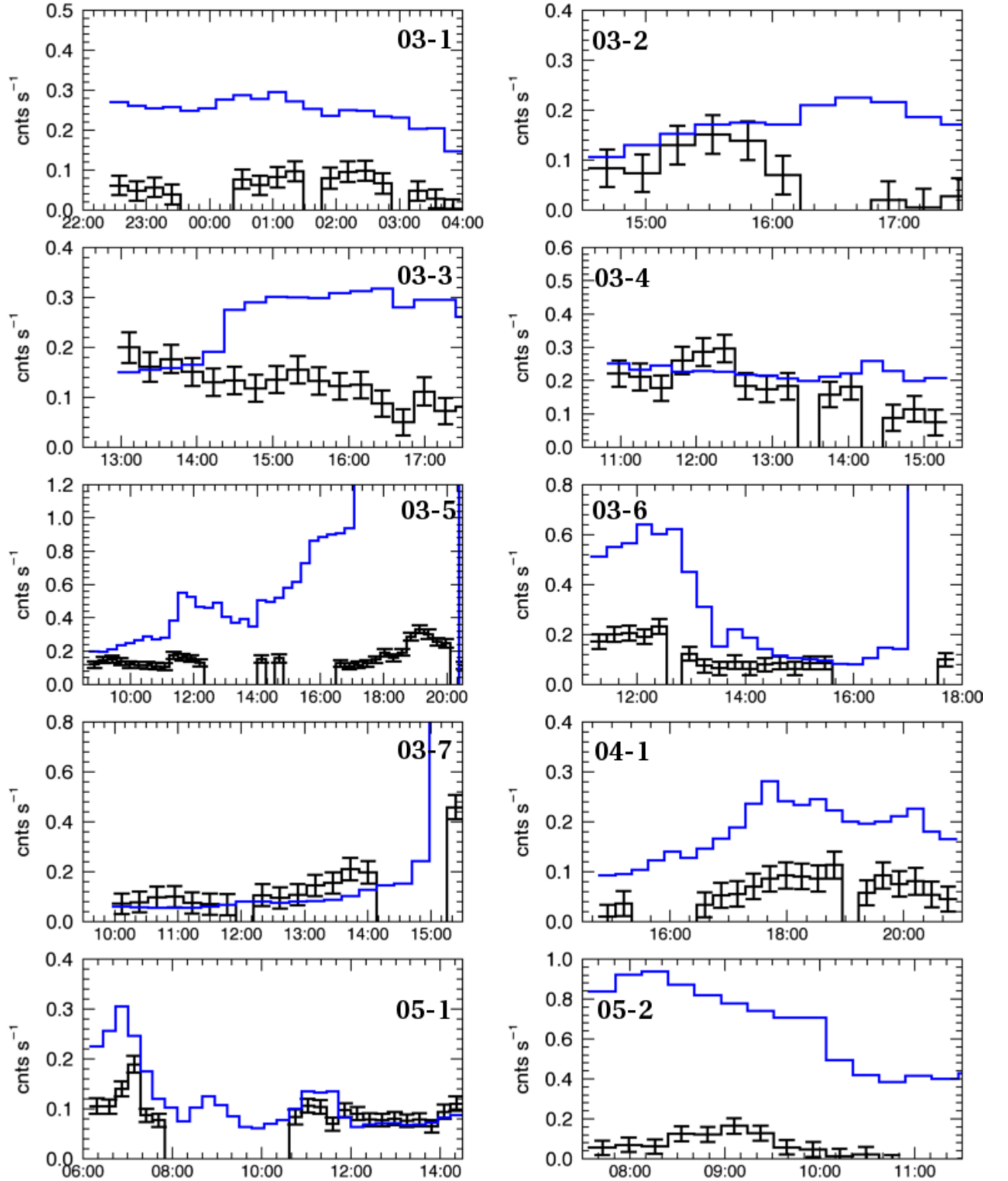


Figure 8. Cases 10-19 of the study using a constant O/H ratio, each panel shows the GUMCIS-4 estimated count rate in blue and the EPIC observations in black with the combined observational and background error bars included.

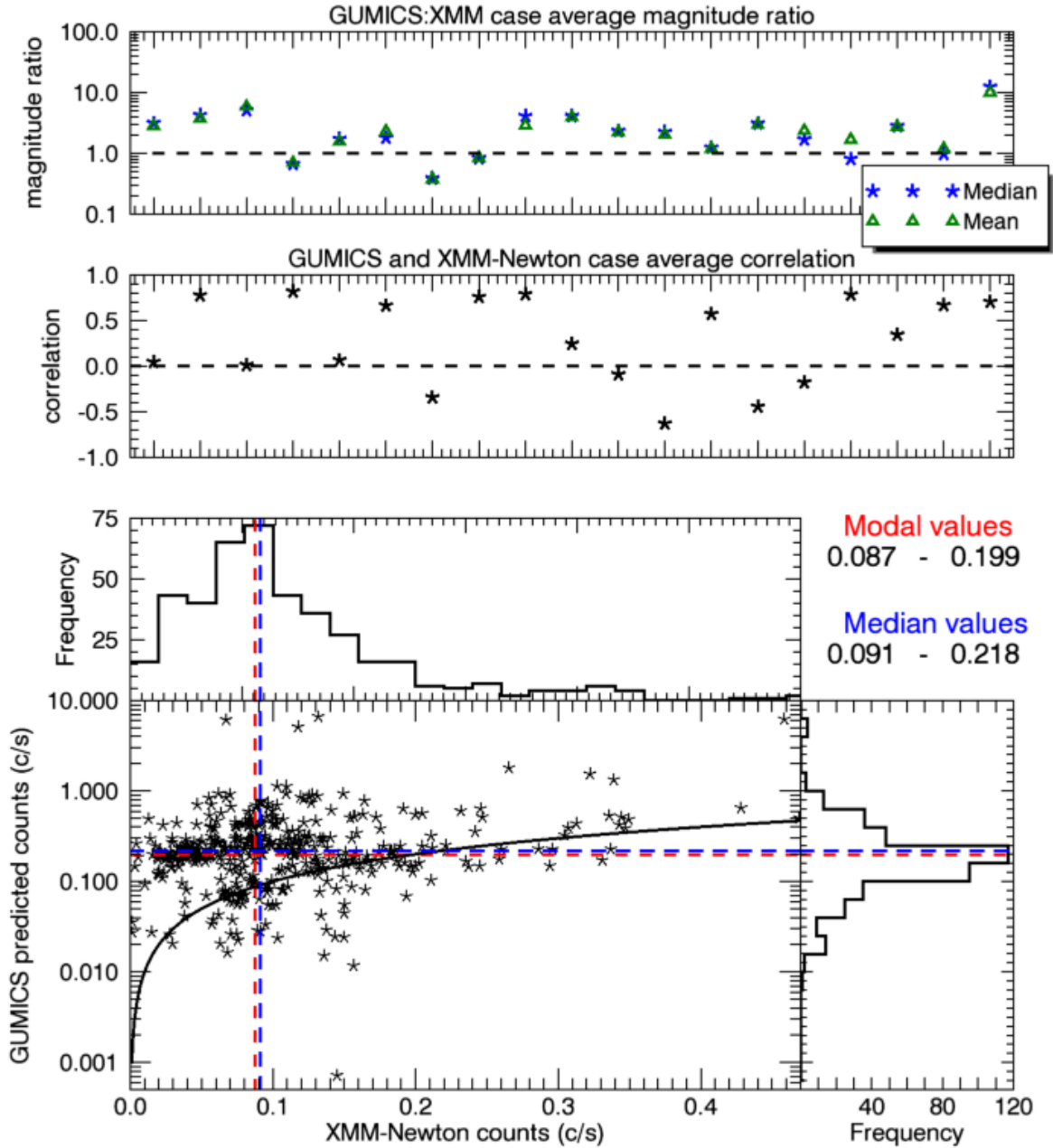


Figure 9. A comparison of the observed and modeled count rates for each case, using the constant modal O/H value from Figure 5. The top panel uses the mean and median magnitude for each case and takes the ratio of the modeled to the observed magnitudes, with the dashed line showing the equal magnitude line. Data points below this line show a lower modeled than observed average magnitude. The middle panel shows the correlation between modeled and observed counts. The lower panel is a scatter point of all data points, with histograms included for both the modeled and observed count distributions. The red and blue dashed lines show the modal and median lines respectively, the solid black dashed line shows the $y=x$ line.

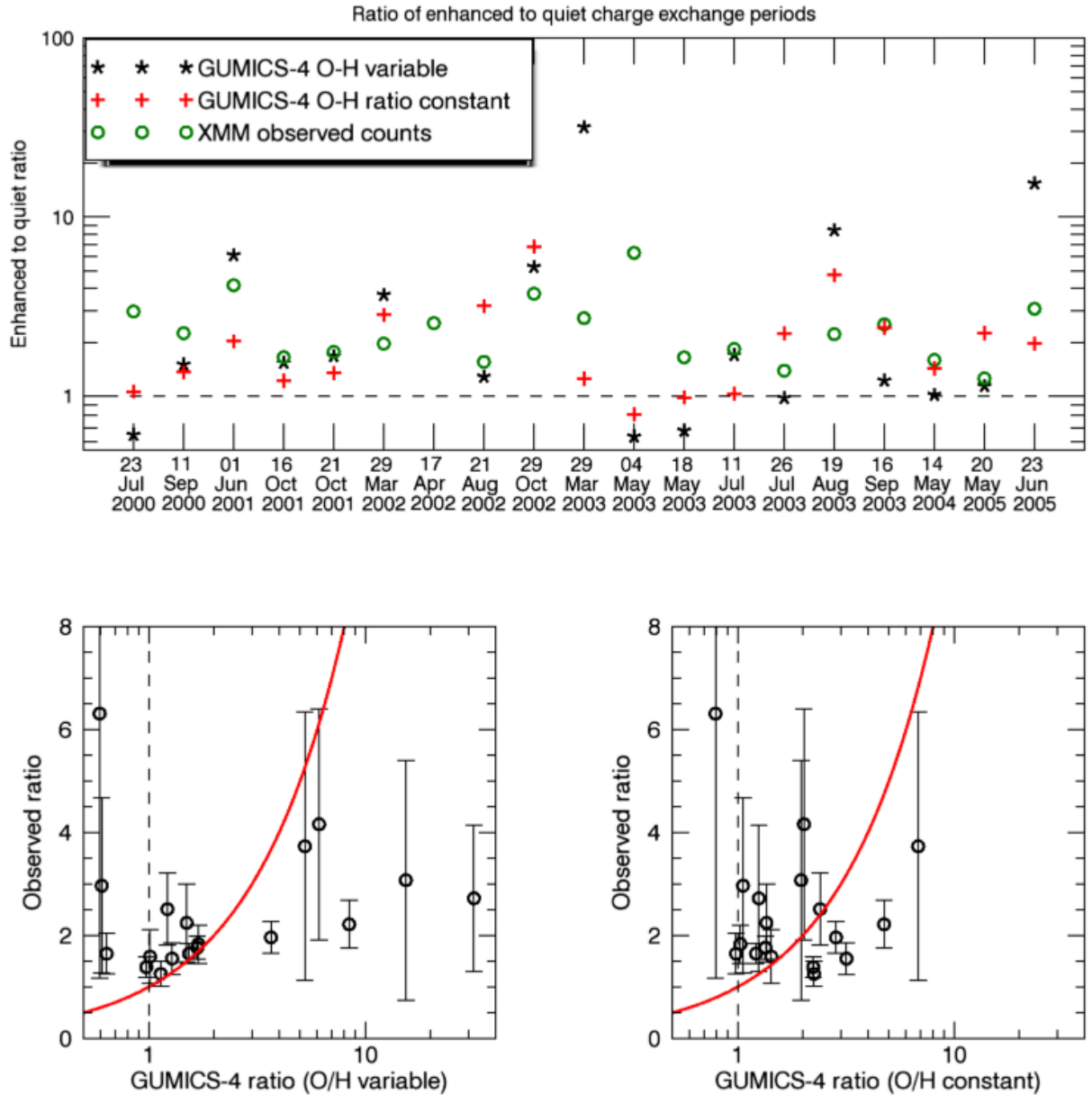


Figure 10. The ratio between the enhanced and quiet charge exchange periods of the lightcurve. The top panel shows the ratio for the O/H varying model data (*), O/H constant model data (+) and the observed data (o). These are in date order to determine any temporal bias. The lower left panel shows a scatter plot of O/H varying model data against the observed data, with the red solid line showing the $y=x$ line. The error bars on the observed data have been propagated from the background and observational data. The lower right panel shows the same plot but with the O/H constant data points.

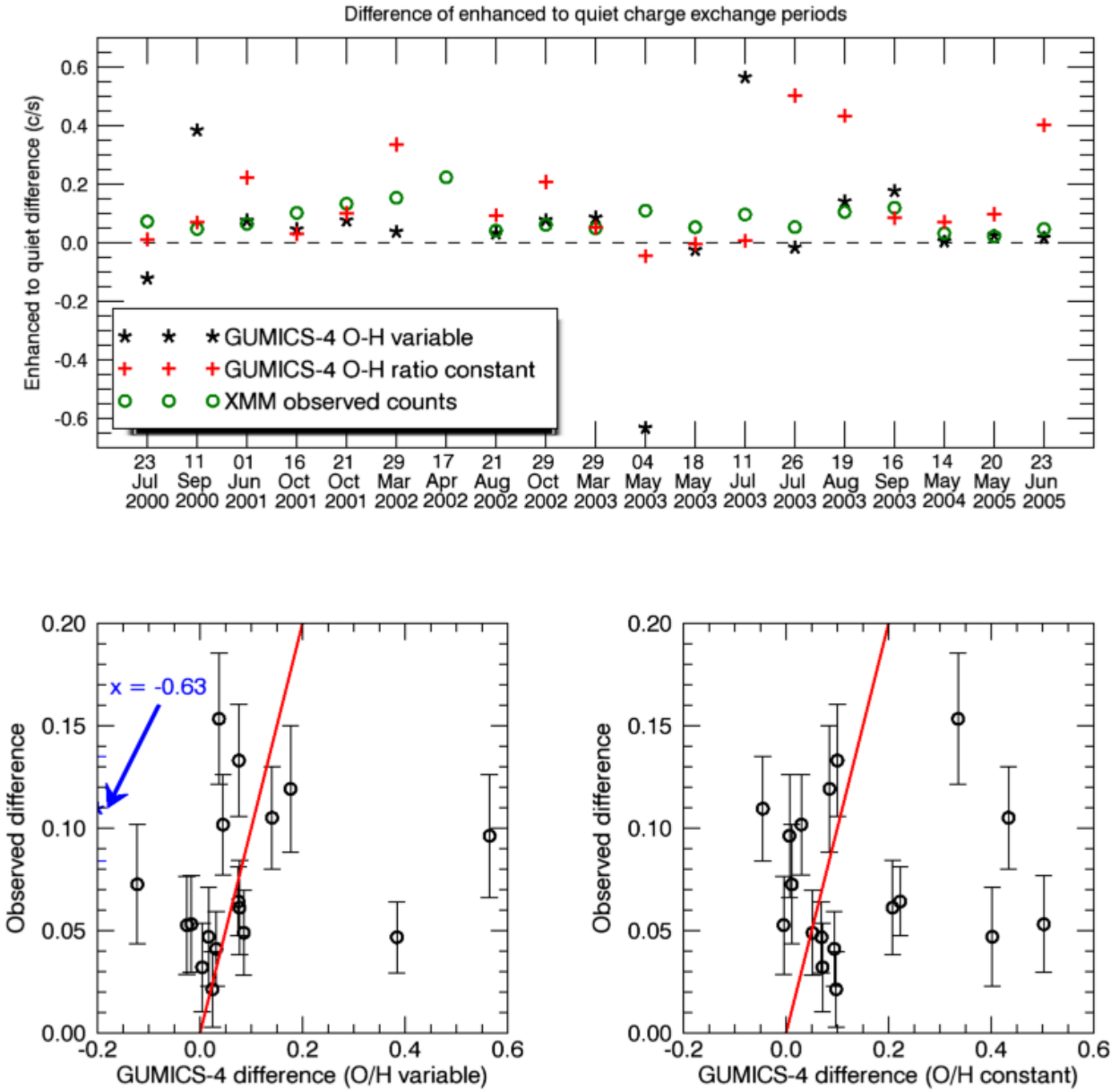


Figure 11. The difference between the enhanced and quiet charge exchange periods of the lightcurve. The top panel shows the ratio for the O/H varying model data (*), O/H constant model data (+) and the observed data (o). These are in date order to determine any temporal bias. The lower left panel shows a scatter plot of O/H varying model data against the observed data, with the red solid line showing the $y=x$ line. The error bars on the observed data have been propagated from the background and observational data. The lower right panel shows the same plot but with the O/H constant data points.

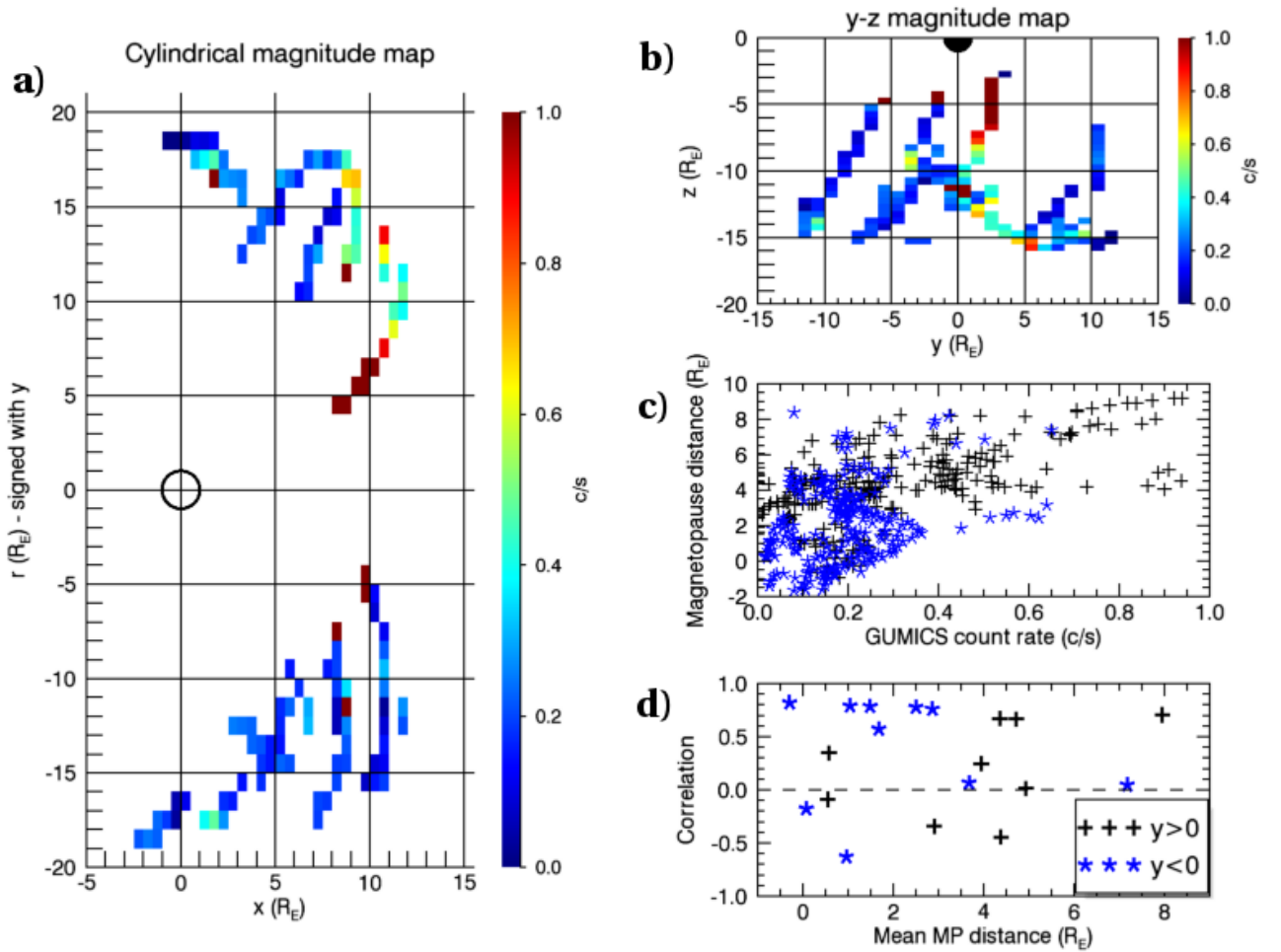


Figure 12. The distribution of GUMICS-4 count rate distribution. **a)** A cylindrical plot in the x - r plane with r signed by y showing the average modeled count rate in each bin, based on the position of XMM-Newton. **b)** The count rates binned in the y - z plane. **c)** A scatter plot showing the GUMICS-4 count rate values against distance from the magnetopause. **d)** The correlation between GUMICS-4 and observations for each case plotted against the average distance from the magnetopause.

Table 1. List of the XMM-Newton observation cases used in this study. The mean case magnitude, pre background removal, is included as well as the calculated background value, both in c/s and as a percentage of the case magnitude. Rejected cases are due to the instrument pointing into the nightside of the Earth where we don't use the MHD model.

Case	Revolution	Obs ID	Date	Duration (hrs)	Magnitude ¹ (c/s)	Background (c/s)
2000						
00-1	0114	0127921101	23 Jul	2.5	0.319	0.129 (40.4%)
00-2	0139	0109060101	11 Sep	14.5	0.146	0.048 (33.2%)
2001						
01-1	0271	0111550401	01 Jun	26.5	0.179	0.050 (28.1%)
01-2	0339	0054540501	16 Oct	6.5	0.300	0.032 (10.9%)
01-3	0342	0085150301	21 Oct	9	0.306	0.059 (19.2%)
2002						
02-1	0422	0113050401	29 Mar	7.5	0.444	0.101 (22.8%)
02-2	0431	0136000101	17 Apr	6	0.298	0.077 (25.9%)
02-3	0494	0109120101	21 Aug	11	0.165	0.038 (23.0%)
02-4	0529	0147540101	29 Oct	7	0.232	0.089 (38.5%)
2003						
03-1	0605	0146390201	29 Mar	6.5	0.215	0.077 (35.6%)
03-2	0623	0150610101	04 May	3	0.288	0.107 (37.2%)
03-3	0630	0143150601	18 May	5.5	0.291	0.080 (27.7%)
03-4	0657	0141980201	11 Jul	6	0.398	0.107 (27.0%)
03-5	0664	0150680101	26 Jul	13	0.268	0.059 (22.0%)
03-6	0676	0049540401	19 Aug	7	0.254	0.082 (32.2%)
03-7	0690	0149630301	16 Sep	5.5	0.331	0.116 (35.0%)
2004						
04-1	0811	0202100301	14 May	7	0.228	0.079 (34.6%)
2005						
05-1	0997	0303260501	20 May	9.5	0.164	0.037 (22.4%)
05-2	1014	0305920601	23 Jun	7	0.267	0.105 (39.4%)
Rejected cases						
	0151	0094800201	05 Oct	2000		
	0163	0100640201	29 Oct	2000	²	
	0178	0110980101	27 Nov	2000	²	
	0178	0101040301	28 Nov	2000	²	
	0209	0093552701	28 Jan	2001		
	0279	0070340501	18 Jun	2001		
	0505	0153752201	11 Sep	2002	²	
	0645	0150320201	17 Jun	2003		
	0906	0203361501	19 Nov	2004	²	
	0982	0306700301	19 Apr	2005		
	1199	0402250201	27 Jun	2006		

D R A F T

February 12, 2016, 2:39pm

D R A F T

¹ Mean case magnitude before background removal.

² The pointing direction is away from the datacube, providing no data. However, the case can still be used for solar wind information.